Three-dimensional modeling of Mount Vesuvius with sequential integrated inversion

Rosaria Tondi and Roberto de Franco

Istituto per la Dinamica dei Processi Ambientali, Consiglio Nazionale delle Ricerche, Milan, Italy

[1]   A new image of Mount Vesuvius and the surrounding area is recovered from the tomographic inversion of 693 first P wave arrivals recorded by 314 receivers deployed along five profiles which intersect the crater, and gravity data collected in 17,598 stations on land and offshore. The final three-dimensional (3-D) velocity model presented here is determined by interpolation of five 2-D velocity sections obtained from sequential integrated inversion (SII) of seismic and gravity data. The inversion procedure adopts the "maximum likelihood" scheme in order to jointly optimize seismic velocities and densities. In this way we recover velocity and density models both consistent with seismic and gravity data information. The model parameterization of these 2-D models is chosen in order to keep the diagonal elements of the seismic resolution matrix in the order of $0.2-0.8$. The highest values of resolution are detected under the volcano edifice. The imaged 6-km-thick crustal volume underlies a 25×45 km^2 area. The interpolation is performed by choosing the right grid for a smoothing algorithm which prepares optimum models for asymptotic ray theory methods. Hence this model can be used as a reference model for a 3-D tomographic inversion of seismic data. The 3-D gravity modeling is straightforward. The results of this study clearly image the continuous structure of the Mesozoic carbonate basement top and the connection of the volcano conduit structure to two shallow depressions, which in terms of hazard prevention are the regions through which magma may more easily flow toward the surface and cause possible eruptions.   *INDEX TERMS:* 8180 Tectonophysics: Tomography; 8499 Volcanology: General or miscellaneous; 1219 Geodesy and Gravity: Local gravity anomalies and crustal structure; 3210 Mathematical Geophysics: Modeling; 3260 Mathematical Geophysics: Inverse theory; *KEYWORDS:* sequential integrated inversion, Sobolev norm, Mount Vesuvius velocity model, Mount Vesuvius density model

Citation: Tondi, R., and R. de Franco, Three-dimensional modeling of Mount Vesuvius with sequential integrated inversion, *J. Geophys. Res.*, *108*(B5), 2256, doi:10.1029/2001JB001578, 2003.

1.   Introduction

[2]   The Somma-Vesuvius volcano complex is a central composite volcano whose existence is due to the subduction under the Greek islands (Hellenic arc) and southern Italy (Calabrian arc) in the context of the convergence between the Eurasian Plate and the northward moving African Plate. It is a central composite volcano formed by an older stratovolcano (Monte Somma, Figure 1) with a summit caldera partially filled by the composite younger cone of Mount Vesuvius. The structure is bordered by Mesozoic carbonate rocks.

[3]   The essential feature of a composite volcano is a conduit system through which magma from a reservoir deep in the Earth crust rises to the surface. The volcano is built up by the accumulation of pyroclastic deposits and material erupted through the conduit and increases in size as lava and ashes are added to its slopes. When a composite volcano becomes dormant, erosion begins to destroy the cone and next the hardened magma filling the conduit. Given the low density of the dominant deposits that characterize these volcanoes, negative gravity anomalies, usually between 10 and 30 mGal are to be expected.

[4]   Several papers and books have been written about this volcano [*Barberi et al.*, 1983; *De Vivo et al.*, 1993; *Santacroce*, 1987; *Scandone et al.*, 1993]. Among Earth's volcanoes, Vesuvius not only has a peculiar geological history, but it is also intimately interwoven with the history of humanity [*Richter*, 1996]. Certainly, the most notable aspect of Vesuvius among Earth's volcanoes is the dense population surrounding it and on its slopes, although the volcano's history suggests that the longer is the quiescence period, the more violent is the next activity. Beginning with the last Subplinian eruption (1631), Vesuvius has displayed Strombolian activity (with open conduit) and effusive-explosive eruptions alternating with short periods of quiescence. The most recent cycle of activity ended with the 1944 eruption, which marked the beginning of a quiescent period characterized by low activity (intracrateral fumaroles and moderate seismic activity). In order to detect in advance significant variations in some parameters which can indicate
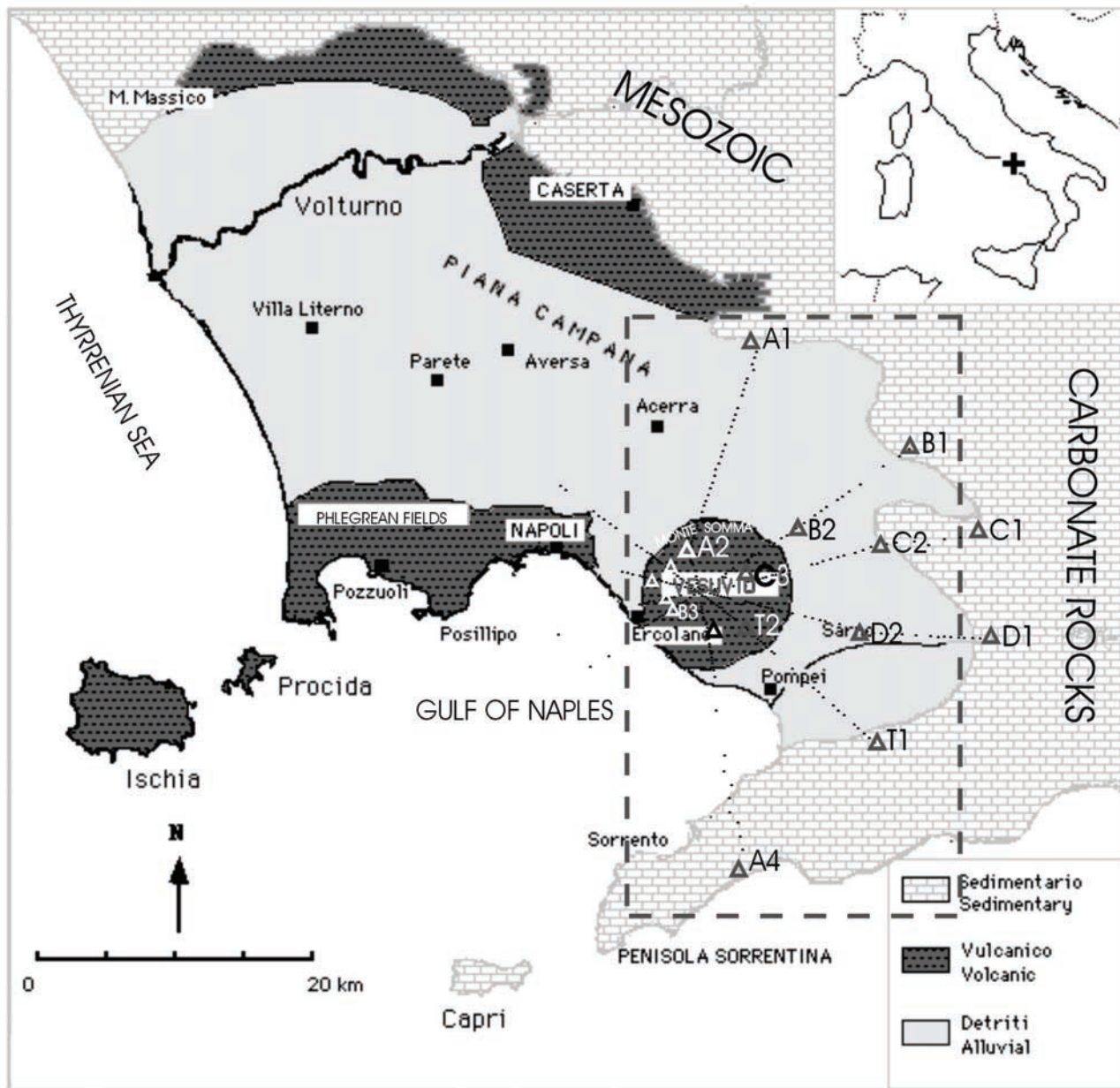
Figure 1. Geologic map of the Somma-Vesuvius region showing the five TOMOVES seismic lines. Triangles are shot points. The studied area by the 3-D model is outlined by a dashed rectangle.

reactivation, Vesuvius is monitored by a comprehensive system of seismic and geodetic networks managed by the Osservatorio Vesuviano.

[5] Seismic and gravity data that we use for our analysis were collected in the framework of the Tomography of Mount Vesuvius (TOMOVES) experiment, an European project aimed at reconstructing the three-dimensional (3-D) image of Mount Vesuvius volcano and the crust underneath, using high-resolution seismic tomography techniques and other geophysical methods [*Gasparini and TOMOVES Group*, 1998].

[6] We obtain our 3-D model in three main steps. First, the first arrival times from seismic signals recorded along five profiles (Figure 1) are picked and inverted for velocity

and interface structure using a 2-D travel time inversion program [*Zelt and Smith*, 1992], in which the value of velocity nodes and depths of boundary nodes are jointly adjusted to obtain a match between the observed and calculated data. Second, the final seismic models are transformed into density models through a node-dependent, velocity-density relationship, and then used for the computation of the gravity anomalies to compare to the observed Bouguer anomaly curves. The reduction of gravity data misfit and the optimization of the density models is performed through the use of the SII procedure [*Tondi et al.*, 2000], an algorithm which allows efficient and reliable joint optimization of velocity and density parameters. As last step, the 2-D images are interpolated by tricubic B splines
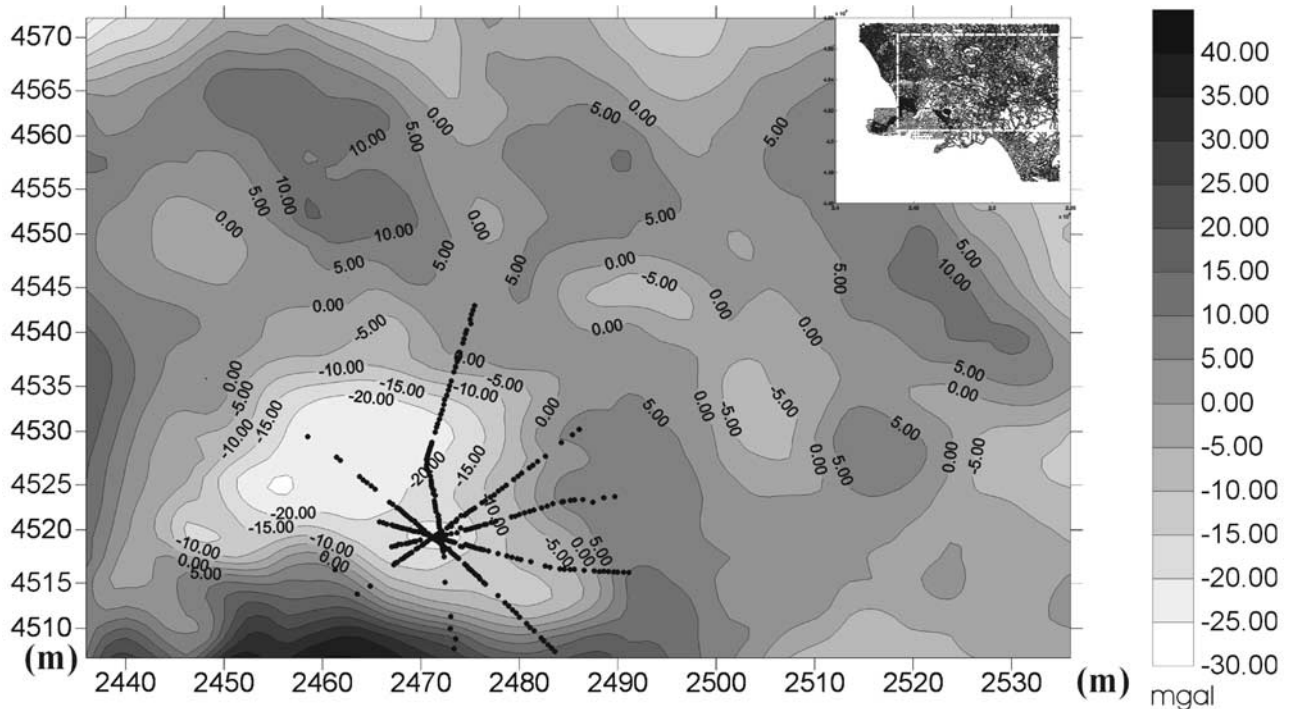
Figure 2. Bouguer anomaly map (density contrast 2.67 g/cm^3) as derived from gravity measurements localized in the inset. Gauss Boaga projection is used for representation, and gravity data, expressed in mGal, are displayed with a contour interval of 5 mGal.

using a smoothing algorithm which creates a model suitable for application of ray-based methods [*Klimeš*, 2000; *Bulant*, 2000; *Žáček*, 2002]. The comparison of observed and predicted 3-D travel time data computed using a numerical ray tracing package [*Červený et al.*, 1988] validate the 3-D interpolated model.

[7] Recent 1-D and 2-D velocity and density models have defined the general structure of the volcanic edifice. Seismic reflection lines have evidenced some E-W and NW-SE striking Quaternary faults, SE of Mount Vesuvius [*Bruno and Rapolla*, 1999]. These are likely to cross beneath the volcano complex and may have some influence on the future volcanic activity. Evidence of a high-velocity body (V_p = 3–4.5 km/s) under the northwestern flank of the volcano is given by the 2-D seismic analysis [*De Matteis et al.*, 1997] of data collected along profile T (Figure 1). Its presence is also indicated by a strong magnetization (∼3 A/m) still present at ∼2000 m but which becomes weak down to 4–5 km below sea level [*Fedi and Rapolla*, 1999]. This body may represent a buried subvolcanic structure (dikes complex and/or thick compact layers). The small evidence for termometamorphosed volcanic rocks among Mount Vesuvius ejecta, rules out the possibility that they may be a significant component of the high-velocity body. Seismic studies along the other profiles of TOMOVES experiment [*de Franco et al.*, 1999] allowed the definition of the geometry of three main geological structures in the area: the polygenic filling of the tectonic depression of the Campanian Plain (*P* wave velocities ranging from 1.5 to 3.0 km/s and densities of 2 g/cm^3); an underlying layer, mainly carbonates and submarine lavas (*P* wave velocities ranging from 3.0 to 5 km/s and densities from 2.2 to 2.4 km/s), and a

limestone unit (with *P* wave velocities higher than 5 km/s and densities higher than 2.4 km/s). The quantitative interpretation of the gravity anomaly [*Berrino et al.*, 1998] provided information about the shape and depth of the sedimentary carbonate basement. Beneath the Somma-Vesuvius the thickness of the basement is about 11 km, and its top is 2 km deep.

[8] A 3-D *P* wave velocity model was obtained by the interpolation of shallow (up to 3–4 km depth) 2-D velocity sections obtained from the nonlinear tomographic inversion of the seismic data we used in our analysis [*Lomax et al.*, 2001]. It allowed the relocation of 400 earthquakes under Somma-Vesuvius volcano concentrated within ∼1 km of the Gran Cono crater axis, at depths of about 1 to 3.5 km below sea level (bsl). This axial cone distribution of background seismicity at these depths is explained through the combined effects of shear stress increase around the zone where the largest change in rock rigidity is expected, i.e., the carbonate top discontinuity, and rock strength weakening due to the dense fracturing associated with magma ascent to the surface during the eruption episodes.

[9] Our final 3-D model confirms previous studies and highlights new results about the structure. First of all, we have a complete 3-D image of Mount Vesuvius up to 6 km of depth. Identifying velocities higher than 5.0 km/s we can contour the depth of the Mesozoic carbonate basement top. This surface is consistent with a borehole drilled by AGIP at Trecase on the SE slope of Somma-Vesuvius and is a continuous structure resembling in shape a saddle for the volcano edifice. The joint analysis of seismic and gravity data evidence a negative velocity anomaly percentage higher than 2% which connects the southern faulted struc-
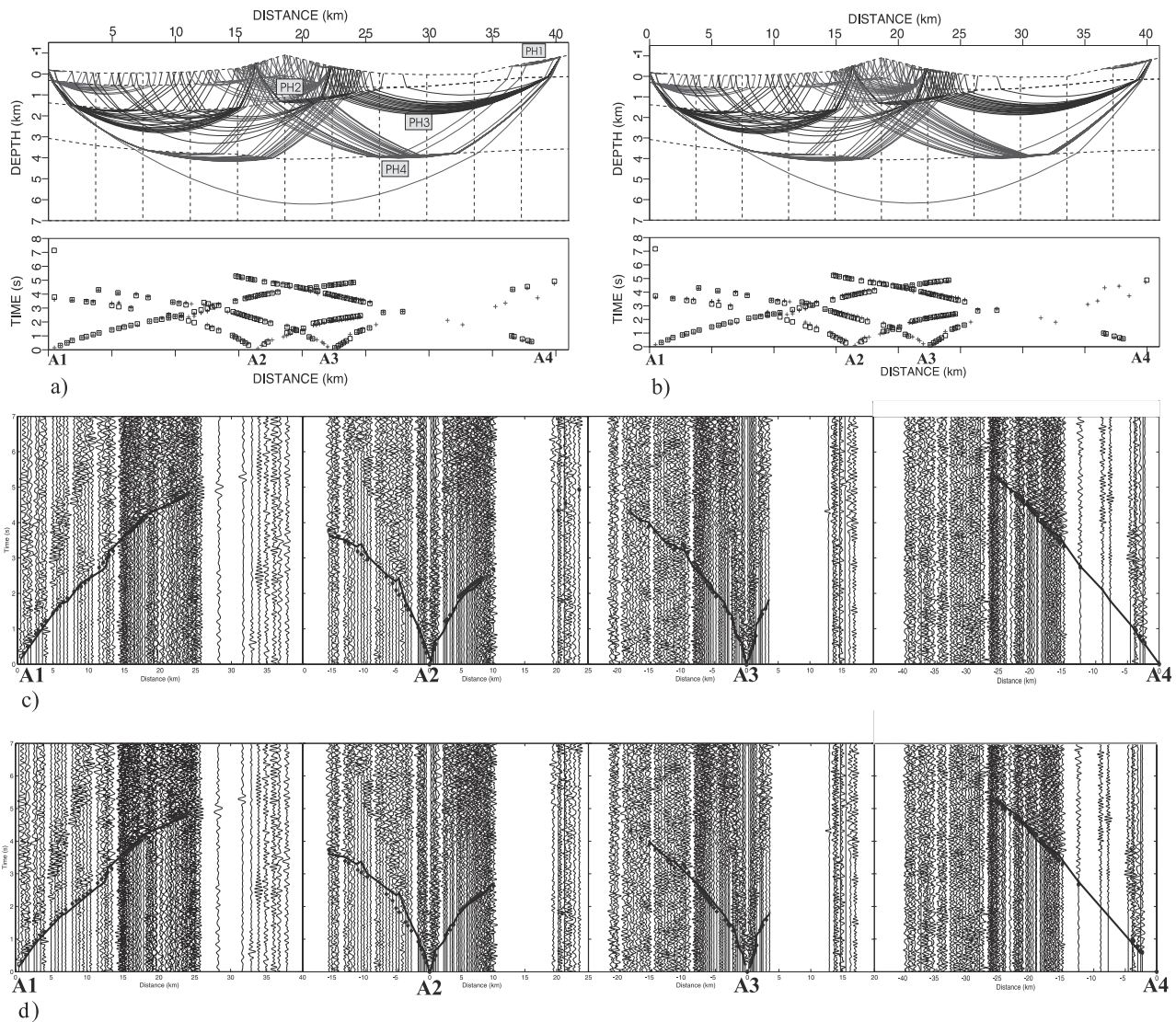
Figure 3. Profile A ray coverage plus observed (pluses) and calculated (squares, points connected with a line on the seismic section) travel times of the final velocity model as recovered after (a, c) seismic travel time inversion and (b, d) SII (see Figure 7 for contoured velocity models). Identification of ray phases is indicated.

ture characterized by velocity and density lows to the volcano feeding system and to the northeastern depression inferred by our 3-D seismic analysis and that conducted by *Lomax et al.* [2001].

2. Data

[10] The main target of the TOMOVES experiment was the 3-D modeling of the structure of Mount Vesuvius and the underlying upper crust with emphasis on the delineation of possible magma reservoirs of significant size (more than 1 km in diameter). Unfortunately, the extremely high urbanization of the investigated area prevented a very dense source and receiver coverage of the target area. The chosen acquisition geometry was a 2-D multiconfiguration.

[11] Seismic data collected along profile T are part of a first stage, performed in 1994, aimed at determining the feasibility of a 3-D tomography of the volcano [*Zollo et al.*,

1996]. Profile T consisted of a 30 km long NW trending seismic line passing through the center of Mount Vesuvius (Figure 1). Seismic energy was generated with about 400 kg of explosive in three inland sites along the profile. The signals were recorded by 82 (60 digital 3C) receivers deployed along the profile with a spacing of 250 m on the volcano and 500 m elsewhere. A linear array consisting of 47 vertical geophones was deployed at the top of the volcano. In 1996, 14 on-land shots were generated along two pairs of quasi-orthogonal profiles (A–C and B–D configuration), 24 to 40 km long, which intersect at the Mount Vesuvius crater, and 140 digital seismic stations were deployed in the field (Figure 1). Along each profile the station spacing was variable from 250 m in the inner part across Mount Vesuvius to 500 m outside. The largest explosions were carried out at the profiles ends, on Mesozoic carbonate outcrops, since the results of 1994 campaign had showed that high-energy shots on limestone
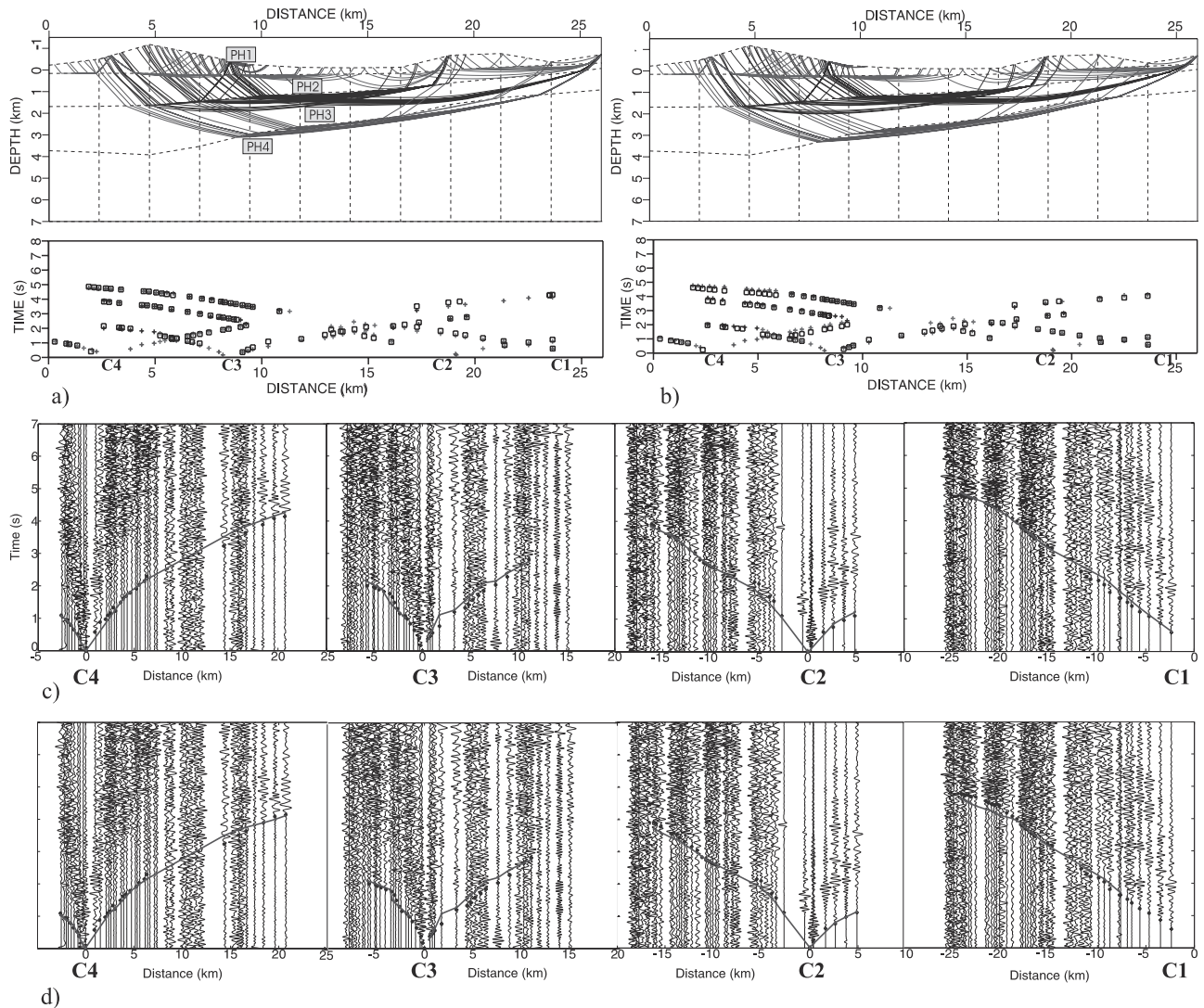
Figure 4. Profile C ray coverage plus observed (pluses) and calculated (squares, points connected with a line on the seismic section) travel times of the final velocity model as recovered after (a, c) seismic travel time inversion and (b, d) SII (see Figure 7 for contoured velocity models). Identification of ray phases is indicated.

outcrops produce seismic waves which penetrate down to at least 10–12 km. For a detailed description of the complete experiment, see *Gasparini and TOMOVES Group* [1998].

[12] The gravity map of the area (Figure 2), which covers all the Campanian plain and the Gulf of Naples, was obtained from 17,598 stations. It was derived from the integration of quality checked and reanalyzed previously measured on-land data [*Berrino et al.*, 1998] with new gravity data collected offshore and along selected profiles in the Vesuvian area (TOMOVES Group).

3. Method

3.1. Seismic Travel Time Inversion

[13] The selection of seismic events to be used for the inversion procedure was rather difficult. Volcanic rock exhibits considerable seismic attenuation, bad geophone-earth coupling and low shot efficiency. Moreover, the investigated area is densely populated, and as a consequence, the seismic records are often noisy.

[14] Four first-arrival travel time phases are identified by their velocity and spatial relationships along the profiles (Figures 3 and 4 for profiles A and C): (1) phase P1 with a velocity ranging from 1.5 to 3.0 km/s identifies the volcanic and terrigenous unit; (2) phase P2 with a velocity ranging from 3.0 to 5 km/s identifies the carbonates and submarine lavas; (3) phase P3 with a velocity ranging from 5 to 6.3 km/s identifies the limestone unit; and (4) a limited number of first arrivals are observed with a velocity greater than 6.3 km/s (phase P4 in profiles A and C). These are interpreted as refractions through denser limestone at depths greater than 4 km.

[15] First-arrival travel time picks are made from all the receiver gathers. In order to improve the signal-to-noise ratio we apply a band-pass, Butterworth, zero-phase shift filter with frequency limits depending on trace spectra (3–15 Hz). After picking and classifying the arrivals of the phases
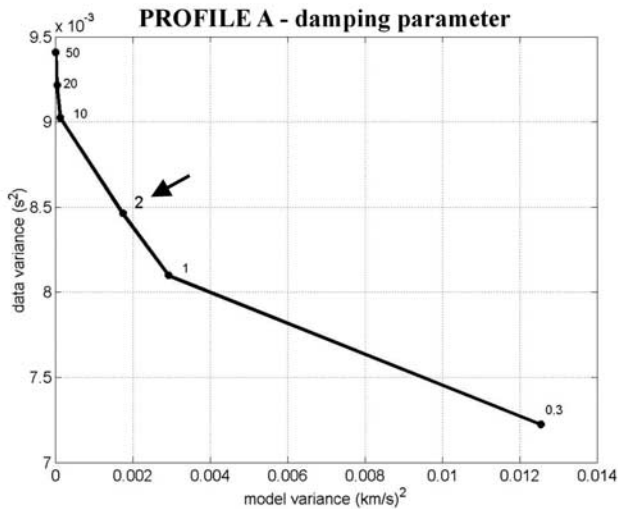
Figure 5. Data variance versus model variance for the velocity parameter of the seismic final model A. The arrow indicates the chosen value of damping factor [*Menke*, 1984]. This value is used for the subsequent SII.

described above, estimates of the pick uncertainties are required to allow for the appropriate data fitting and weighting during travel time inversion. We define three types of errors: (1) travel time picking uncertainty; (2) random errors which account for the variance of the trigger response; and (3) errors associated to nonlinear shot-receiver geometries. For each pick the travel time picking uncertainty value is qualitatively estimated on the basis of the signal-to-noise ratio and coherency of the first arrivals; the uncertainties range from 0.05 to 0.1 s. To estimate the error associated to the variance of the trigger response, we consider a maximum time lag of 200 ms in 24 hours and compute an error proportional to the time picked. To apply a 2-D modeling approach, it is necessary to account for the deviation of the shot-receiver geometry from a line. For profile A, this is accomplished, by fitting a least squares line to the receiver sites and projecting each shot location perpendicularly onto the line. The receiver sites are projected onto the line by leaving unchanged the true source-receiver offsets for subsequent modeling. Therefore a particular receiver site will generally have a different position along the line for each shot. The maximum deviation detected between the true site and the represented site is of 0.56 km, which is much less than the average lateral resolution of the data, as described below. Considering an average velocity of 3.5 km/s, an uncertainty is assigned, taking into account the spatial relative deviation of each receiver from each shot (σ is deviation/average velocity).

[16] The initial models are obtained using the procedure of intercept travel time and of reduced travel time curves proposed by *Pavlenkova* [1973] and modified by *Luzio et al.* [1983]. This procedure performs the transformation of the observed travel time curves into intercept time sections then converted into depth sections [*Pavlenkova*, 1982]. The elevation of each shot and receiver site, determined using GPS, is sampled such as the top layer boundary of the five models.

[17] These starting models, consisting of a small number of velocity and boundary nodes for each layer are used to begin a "layer stripping" approach used to model the data with an iterative DLSQR technique [*Zelt and Smith*, 1992]. With this procedure we model the data in two steps; shallower model layers being fixed for subsequent step: (1) P1 and P2 constrain the first boundary and shallower velocity structures; and (2) P3 and P4 constrain the carbonate discontinuity and velocity gradients in the deepest layer. At each step, (1) the damping parameter is chosen empirically, by evaluating the trade-off curve of model variance (squared difference of the velocity parameter adjustment vector) against data variance [*Menke*, 1984; *Eberhart-Phillips and Reyners*, 1986]; (2) the resolving power of the travel times involved in the reconstruction of the velocity field is assessed; and (3) nodes are added where necessary to improve the fit with the data, while maintaining a sufficiently high resolution of the model parameters. In order to illustrate our choice of damping factors, we show the diagram of trade-off curve related to profile A in Figure 5. As the damped least squares solution can be interpreted as the inverse that minimizes a weighted combination of data variance and model variance size, we select the value (2 in this case) at which we can detect a change in the curve gradient in a point with the minimum data variance associated to an acceptable model variance. Given a linearized seismic inverse problem, one very rough estimate of the illumination of the model space is given by the hit count, which sums up the number of rays which contribute to the solution at a node. This estimate, together with the evaluation of the diagonal elements of the resolution matrix (RDEs), which quantify the amount of independence of a model parameter solution, indicate the resolving power of the data set in the model [*Haslinger et al.*, 1999; *Kissling et al.*, 2001]. RDEs are strictly dependent on the choice of damping factors: the larger these are, the lower becomes the value of RDEs. In this way we control the correctness of our choice in point 1: in areas that are relatively poorly sampled, a low damping value may produce velocity artifacts, which should be avoided. In Figures 6a, 6b, 6c, 6d, and 6e, we summarize diagrams of hit counts and RDEs for the final models along the five profiles. As the total number of travel times used for each profile is not high (see Table 1 for more details), for the chosen parameterization (average resolution length of 4 km) and damping, we choose to define the solution as reliable if the RDE is greater than 0.2 and hit counts higher than 10. As indicated by the diagrams this is observed in profile A, between 0 and 30 km, up to a depth of 4 km; in profile B, between 6 and 22 km, up to a depth of 2 km; in profile C, between 0 and 12 km, up to a depth of 2 km; in profile D, between 0 and 20 km, up to a depth of 2 km; in profile T, between 7 and 22 km, up to a depth of 2 km.

[18] A diagram of the spread function (SF) [*Eberhart-Phillips*, 1986; *Eberhart-Phillips and Reyners*, 1997] is also represented in order to observe how the information for each node is smeared. The spread function compresses each row of the resolution matrix into a single number that describes how strong and peaked the resolution is for that node. SF is generally low, in the order of 0.25 or lower. Only in profile A we observe high values of SF, between 30 and 41 km, corresponding to low values of RDEs. The models are para-
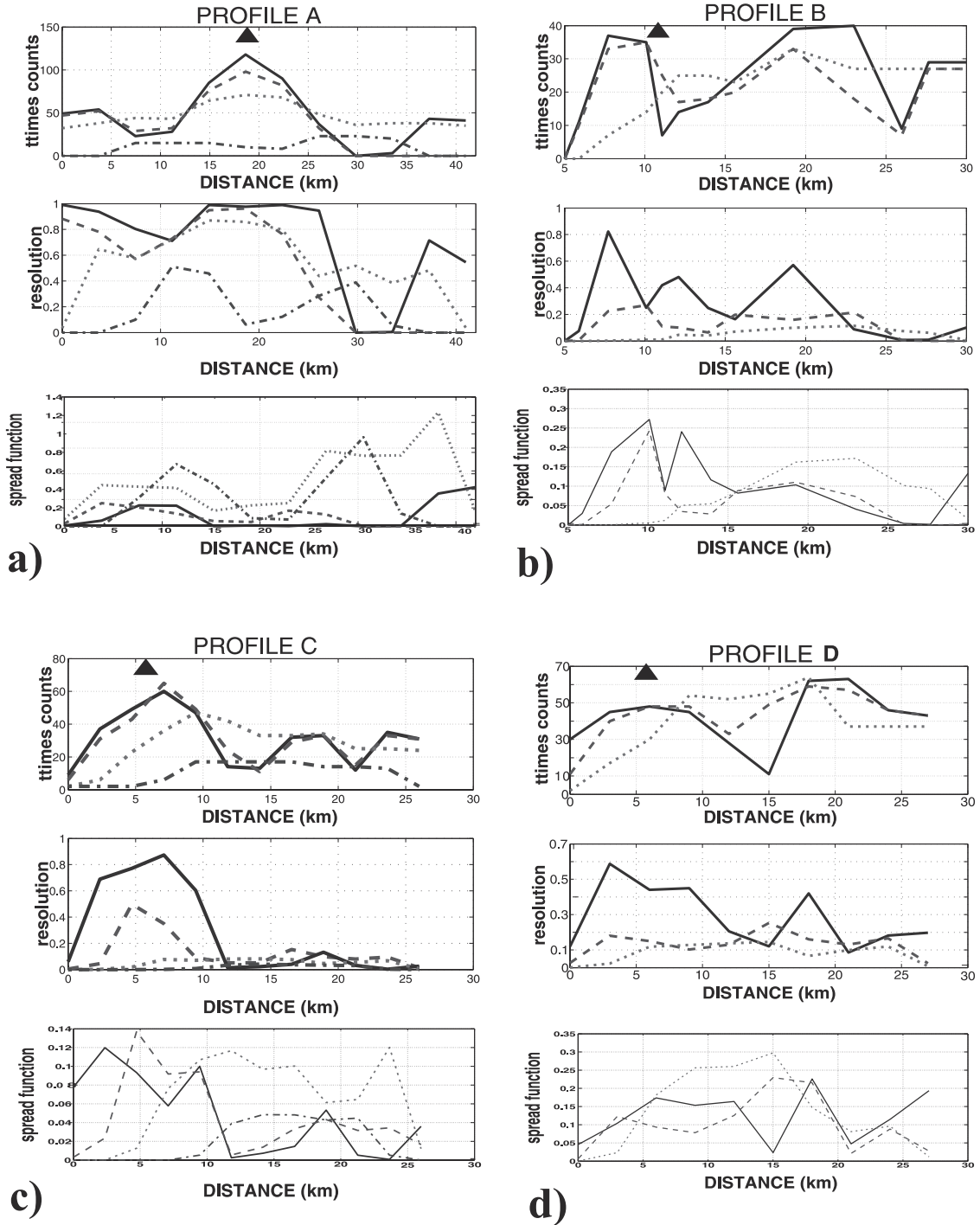
Figure 6. (top) Hit counts, (middle) diagonal elements of resolution, and (bottom) spread function separated for each layer (solid line for the first layer, dashed line for the second layer, dotted line for the third layer, dash-dotted line for the fourth layer) of the velocity parameters associated with each profile. The interpretation of these quantities together is used to derive the area with reliable resolution. The lateral resolution length is 3.7 km for profile A, 2 km for profile B, 2 km for profile C, 3 km for profile D, and 3 km for profile T. Position of Mount Vesuvius is indicated by solid triangle.

meterized with the minimum number of nodes which allows a good travel time fit and ray coverage (Figures 3 and 4 with profiles A and C). Travel time fits are assessed using the normalized form of the misfit parameter χ^2. In general, a value of χ^2 equal to 1 is sought in that this indicates the data have been fit within their assigned uncertainties [*Zelt and*

Forsyth, 1994]. For our models, taking into account problems originating from the three-dimensional Earth structure and the non linear shot-receiver geometry, we assume a good fit for a value of χ^2 ranging from 1 to 5 (Table 1). Table 2 summarizes the boundary nodes resolution of the final models. Independently of resolution, all profiles
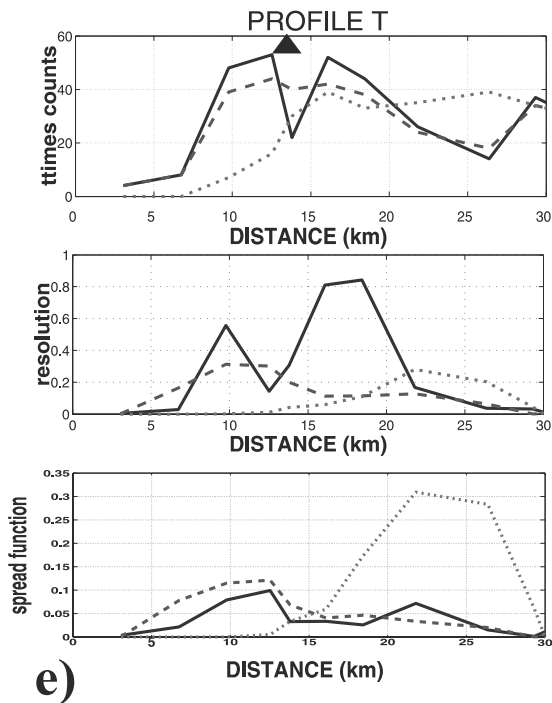
e)

Figure 6. (continued)

(Figures 7a, 7c, 7e, 7g, and 7i) are uniformly extended up to depths of 7 km, in order to make use of the information provided by gravity data in those areas poorly or not at all resolved by seismic rays. We have shown [*Tondi et al.*, 2000] that SII is of great use when seismic information is lacking and the additional information (if gravity measurements are reliable) is always consistent with the true model.

3.2. Sequential Integrated Inversion

[19] As our target is the investigation of the shallow structure of Mount Vesuvius up to depths of 7 km, the contribution of deep structures is subtracted from the gravity field measurements. This contribution is calculated using the collocation filter [*Barzaghi et al.*, 1992] and the information related to offshore air gun shots performed in February 1997 in order to image the crustal discontinuities down to the Moho in the Bay of Naples and beneath Mount Vesuvius and the Phlegraean Fields [*Auger et al.*, 2001; *de Franco et al.*, 2000]. For the computation of Bouguer and terrain effects, a density contrast of 2.67 g/cm^3 is used.

[20] The map of gravity residuals, collected at a 2.5-km-wide interval (shown in Figure 2 with a contour interval of 5 mGal), shows a gravity anomaly ranging from −30 to

Table 1. Number of Observations (Points), RMS Travel Time Residual With Respect to the Observed Data (RMS) and the Corresponding χ^2 Value for Each Profile

	Seismic Model			SII Model		
	Points	RMS, s	χ^2	Points	RMS, s	χ^2
Profile A	168	0.098	2.214	164	0.098	3.040
Profile B	80	0.091	1.977	84	0.111	2.450
Profile C	96	0.137	4.695	97	0.144	5.341
Profile D	119	0.105	2.886	116	0.12	3.018
Profile T	102	0.087	1.586	92	0.154	4.786

Table 2. Corresponding Diagonal Elements of the Resolution Matrix Related to Boundary Nodes for Each Profile

Distance, km	Depth, km	Resolution
	Profile A	
0.000000	0.300000	0.262100
3.730000	0.510000	0.415800
7.450000	0.560000	0.087500
11.180000	0.490000	0.203600
14.910000	0.300000	0.453600
18.640000	0.060000	0.539000
22.360000	0.560000	0.116600
26.090000	0.640000	0.019000
29.820000	0.590000	0.000000
33.550000	0.410000	0.000000
37.270000	0.180000	0.000000
41.000000	0.130000	0.000000
0.000000	1.380000	0.007600
3.730000	1.600000	0.239100
7.450000	1.730000	0.226400
11.180000	1.740000	0.314700
14.910000	1.610000	0.266900
18.640000	1.290000	0.295600
22.360000	1.060000	0.228400
26.090000	0.690000	0.152100
29.820000	0.590000	0.192900
33.550000	0.410000	0.206300
37.270000	0.180000	0.276700
41.000000	0.130000	0.013100
0.000000	3.070000	0.000000
3.730000	3.420000	0.000000
7.450000	3.640000	0.028100
11.180000	3.760000	0.151700
14.910000	3.830000	0.080600
18.640000	4.070000	0.003900
22.360000	4.030000	0.003100
26.090000	3.920000	0.030500
29.820000	3.850000	0.109300
33.550000	3.740000	0.007600
37.270000	3.630000	0.000000
41.000000	3.580000	0.000000
	Profile B	
5.000000	0.300000	0.000000
5.890000	0.260000	0.453500
7.720000	0.130000	0.970100
10.080000	−0.120000	0.877100
11.070000	0.060000	0.903700
12.100000	0.110000	0.812200
13.930000	0.160000	0.670500
15.610000	0.360000	0.697900
19.230000	0.460000	0.832800
23.000000	0.330000	0.661900
25.980000	0.240000	0.143300
27.650000	0.210000	0.000000
30.000000	0.190000	0.000100
5.000000	1.900000	0.000000
5.890000	1.840000	0.000000
7.720000	1.690000	0.098400
10.080000	1.480000	0.242800
11.070000	1.210000	0.409500
12.100000	1.170000	0.291500
13.930000	1.150000	0.437700
15.610000	1.220000	0.018800
19.230000	1.160000	0.466800
23.000000	0.890000	0.435600
25.980000	0.610000	0.114200
27.650000	0.390000	0.067600
30.000000	0.280000	0.515900
	Profile C	
0.000000	0.160000	0.369400
2.360000	0.150000	0.942400
4.730000	0.160000	0.126100

Table 2. (continued)

Distance, km	Depth, km	Resolution
7.090000	0.230000	0.388900
9.450000	0.220000	0.655500
11.820000	0.210000	0.400500
14.180000	0.190000	0.568700
16.550000	0.150000	0.537600
18.910000	0.000000	0.500600
21.270000	−0.130000	0.516900
23.640000	−0.220000	0.073300
26.000000	−0.320000	0.170200
0.000000	1.690000	0.000000
2.360000	1.680000	0.011300
4.730000	1.630000	0.167100
7.090000	1.440000	0.294800
9.450000	1.230000	0.393700
11.820000	1.090000	0.118500
14.180000	1.000000	0.000000
16.550000	0.880000	0.262900
18.910000	0.600000	0.335400
21.270000	0.380000	0.000000
23.640000	0.210000	0.010900
26.000000	−0.070000	0.028500
0.000000	3.730000	0.000000
2.360000	3.810000	0.000000
4.730000	3.920000	0.000000
7.090000	3.530000	0.000800
9.450000	2.960000	0.027500
11.820000	2.620000	0.044900
14.180000	2.410000	0.000000
16.550000	2.130000	0.000000
18.910000	1.590000	0.000000
21.270000	1.280000	0.004300
23.640000	1.110000	0.050900
26.000000	0.920000	0.000000
	Profile D	
0.000000	0.170000	0.769700
3.000000	0.200000	0.896000
6.000000	0.380000	0.639600
9.000000	0.490000	0.547700
12.000000	0.490000	0.687700
15.000000	0.470000	0.395900
18.000000	0.440000	0.732800
21.000000	0.390000	0.584400
24.000000	0.310000	0.813200
27.000000	0.190000	0.137400
0.000000	1.500000	0.011300
3.000000	1.520000	0.530900
6.000000	1.540000	0.661100
9.000000	1.740000	0.612400
12.000000	1.620000	0.422200
15.000000	1.440000	0.132500
18.000000	1.240000	0.771700
21.000000	1.000000	0.377100
24.000000	0.760000	0.198500
27.000000	0.430000	0.354800
	Profile T	
3.060000	0.310000	0.056400
6.750000	0.260000	0.410300
9.770000	0.010000	0.634700
12.530000	−0.340000	0.634700
13.800000	−0.160000	0.574200
16.080000	0.210000	0.805600
18.440000	0.680000	0.546200
21.800000	0.720000	0.372000
26.370000	0.220000	0.276100
29.320000	0.110000	0.001300
30.000000	0.100000	0.000500
3.060000	1.630000	0.000000

Table 2. (continued)

Distance, km	Depth, km	Resolution
6.750000	1.500000	0.000000
9.770000	1.190000	0.030300
12.530000	1.080000	0.347600
13.800000	1.190000	0.371100
16.080000	1.220000	0.287100
18.440000	1.270000	0.293500
21.800000	1.600000	0.093000
26.370000	1.130000	0.378800
29.320000	0.150000	0.153700
30.000000	0.240000	0.051500

40 mGal. It is characterized by a strip of high gradients which follows the Appenines, runs almost parallel to the Sorrento peninsula, and turns southwest at the southern sector of the Gulf of Pozzuoli, in a broad gravity minimum [*Berrino et al.*, 1998]. The Somma-Vesuvius is situated on the southern edge of a large gravity minimum north of Naples, corresponding to the Acerra graben [*Cassano and La Torre*, 1987]. The Vesuvian area is characterized by a negative Bouguer anomaly of small extension and amplitude (see observed anomalies along the five profiles in Figure 8).

[21] The subsurface of the final seismic models is divided into cells of variable size and shape corresponding to the trapezoidal cell representation of the 2-D velocity structure [*Zelt and Smith*, 1992], and the initial density models were computed by using different velocity-density relationships which depend on the node velocity: $\rho = 0.7786 * v + 0.3729$ (for velocities ranging from 1.5 to 2.1 km/s), $\rho = 0.1920 * v + 1.6160$ (for velocities ranging from 2.2 to 6.2 km/s), $\rho = 0.2979 * v + 0.9593$ (for velocities ranging from 6.3 to 8.2 km/s) (Nafe and Drake measurements [*Barton*, 1986]) are computed. The gravity curves along the five seismic profiles are extracted by linear interpolation of the Bouguer anomaly map and Talwani's algorithm [*Talwani et al.*, 1959] is used for the forward gravity modeling in order to compare observed to computed anomalies.

[22] The density contrast used for the computation is the same chosen for the estimation of the gravity residual map. The reduction of gravity residuals and the optimization of density models are then performed through the use of the sequential integrated inversion (SII) procedure [*Tondi et al.*, 2000]. In this context, seismic travel times are inverted to obtain the velocities of the final models, and the velocity parameter adjustment vector is used in the algorithm in order to estimate the proper density parameter adjustment vector:

$$\Delta\rho = \left(\mathbf{G}^{\mathrm{T}}\mathbf{C}_{\mathrm{gg}}^{-1}\mathbf{G} + \mathbf{C}_{\mathrm{mm}}^{-1}\right)^{-1}\left(\mathbf{G}^{\mathrm{T}}\mathbf{C}_{\mathrm{gg}}^{-1}\Delta\mathbf{g} + \alpha\mathbf{C}_{\mathrm{mm}}^{-1}\Delta\mathbf{v}\right) \quad (1)$$

where $\Delta\rho = \rho - \boldsymbol{\rho}^0$ is the density parameter adjustment vector; $\Delta\mathbf{g} = \mathbf{g}^{\mathrm{obs}} - \mathbf{g}^0$ is the gravity data residual vector; $\Delta\mathbf{v} = \mathbf{v} - \mathbf{v}^0$ is the velocity parameter adjustment vector; $\mathbf{G}$ is a J by M matrix containing the geometric gravitational coefficients relating each node to each gravity measurement point; $\mathbf{C}_{\mathrm{gg}}$ is the gravity data covariance matrix; and $\mathbf{C}_{\mathrm{mm}}$ is the covariance matrix linked to the assumed relationship between density and velocity.
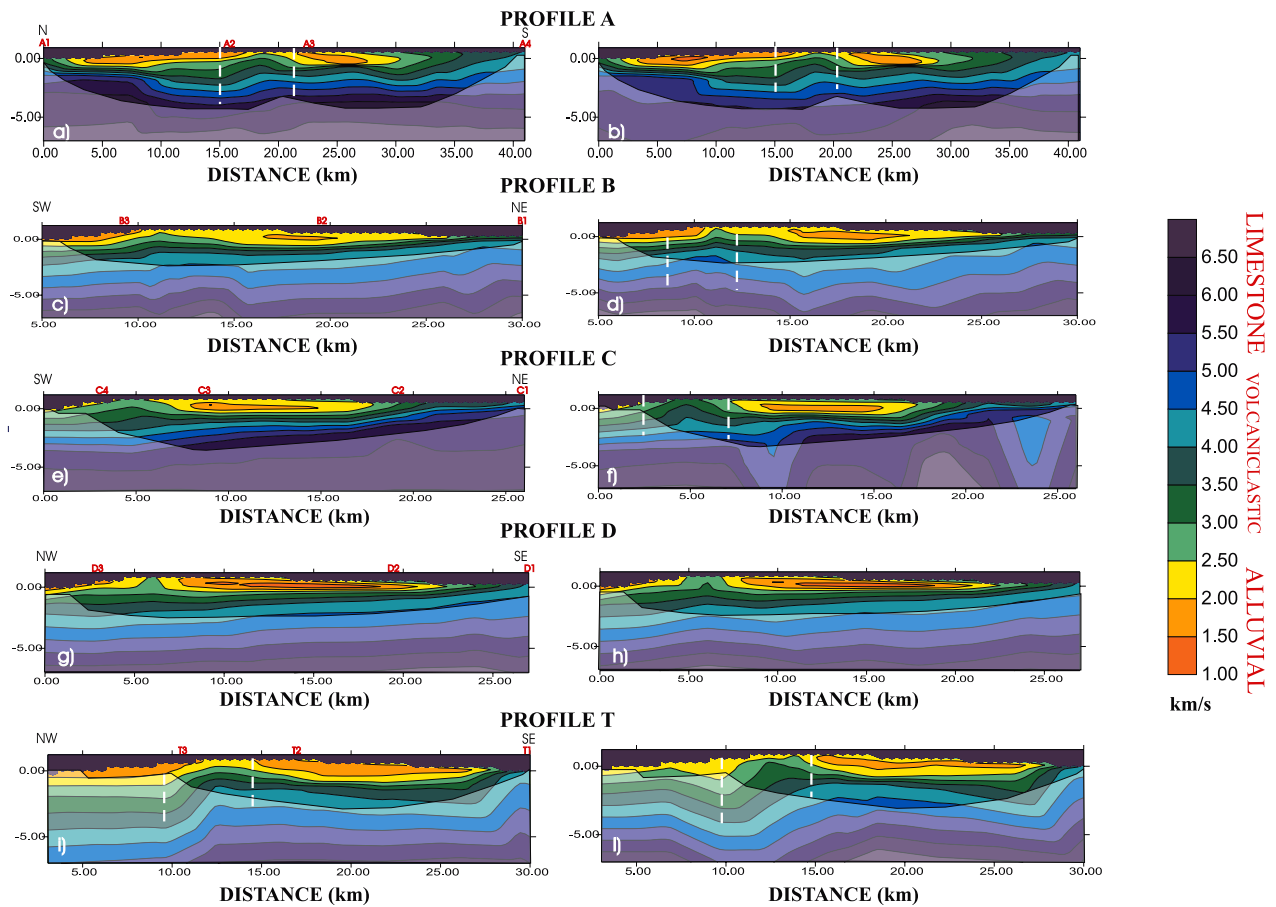
Figure 7. Comparison of velocity solutions for (a, c, e, g, i) seismic and (b, d, f, h, l) SII models. For each seismic profile, shots and geographical information are indicated. Velocity is contoured at 0.500 km/s intervals and related geological structures are indicated. For each profile, areas of resolution lower than 0.1 are white shaded. Between white dashed lines, the shallow high-velocity body is highlighted.

[23] Given the linear ρ-v function: $\rho = \alpha v + \beta$, the $\mathbf{C_{mm}}$ matrix takes into account the error propagation from the velocity to the density model. The error propagation is related to the uncertainty in $\mathbf{v}$ ($\sigma(v_m)$) and to the uncertainties in the coefficients α ($\sigma(\alpha)$) and $\beta(\sigma(\beta))$:

$$\sigma(\rho_m) = v_m\sigma(\alpha) + \alpha\sigma(v_m) + \sigma(\beta) \qquad (2)$$

where $1 \leq m \leq$ number of nodes in the model

[24] Under the assumption that there is no correlation among the errors in each node, the value of $\sigma(v_m)$ is fixed using the square root of the diagonal elements of the a posteriori model covariance matrix estimated by the seismic travel time inversion program. We justify this choice, considering that a posteriori model parameter covariance depends on the data covariance and the way in which the error is mapped from data to model parameters. Tests on synthetic data showed that final densities are better retrieved in this way than those computed by assigning a single mean value to each parameter. The parameters $\sigma(\alpha)$ and $\sigma(\beta)$ are evaluated through a simple least squares analysis on the basis of Nafe and Drake measurements [*Barton*, 1986]. The optimum density parameter adjustment vector is then summed to the initial density vector, densities are converted into velocities and the new velocity models are validated by ray tracing.

[25] Quantitative results of the models with the best seismic χ^2 and the least gravity misfit, achieved after a single SII are shown in Table 3. It can be seen from Table 3 and from the diagrams of the gravity residuals (Figure 8) that while the seismic χ^2 is in the range of that estimated with the seismic travel time inversion and seismic resolution does not undergo any deterioration, there is a significant improvement in the fitting of the gravity curve.

[26] We do not perform additional inversions because we believe that a better result (σ_g smaller) can be achieved only with gravity data being collected with a smaller sampling interval. Gravity residuals are also computed for the density models recovered from the 2-D velocity models which have been used by *Lomax et al.* [2001] to develop the 3-D velocity model used for earthquake locations. The residuals are quite large and density models need to be optimized, especially in those regions with poor seismic resolution (Figure 8).

3.3. The 3-D Velocity Model

[27] We construct a 25 × 45 × 6 km, *P* wave velocity model for Mount Vesuvius and surrounding areas by the interpolation of the 2-D velocity sections recovered by the inversion of seismic travel times and by SII. We build a model without interfaces, limited in the uppermost side by
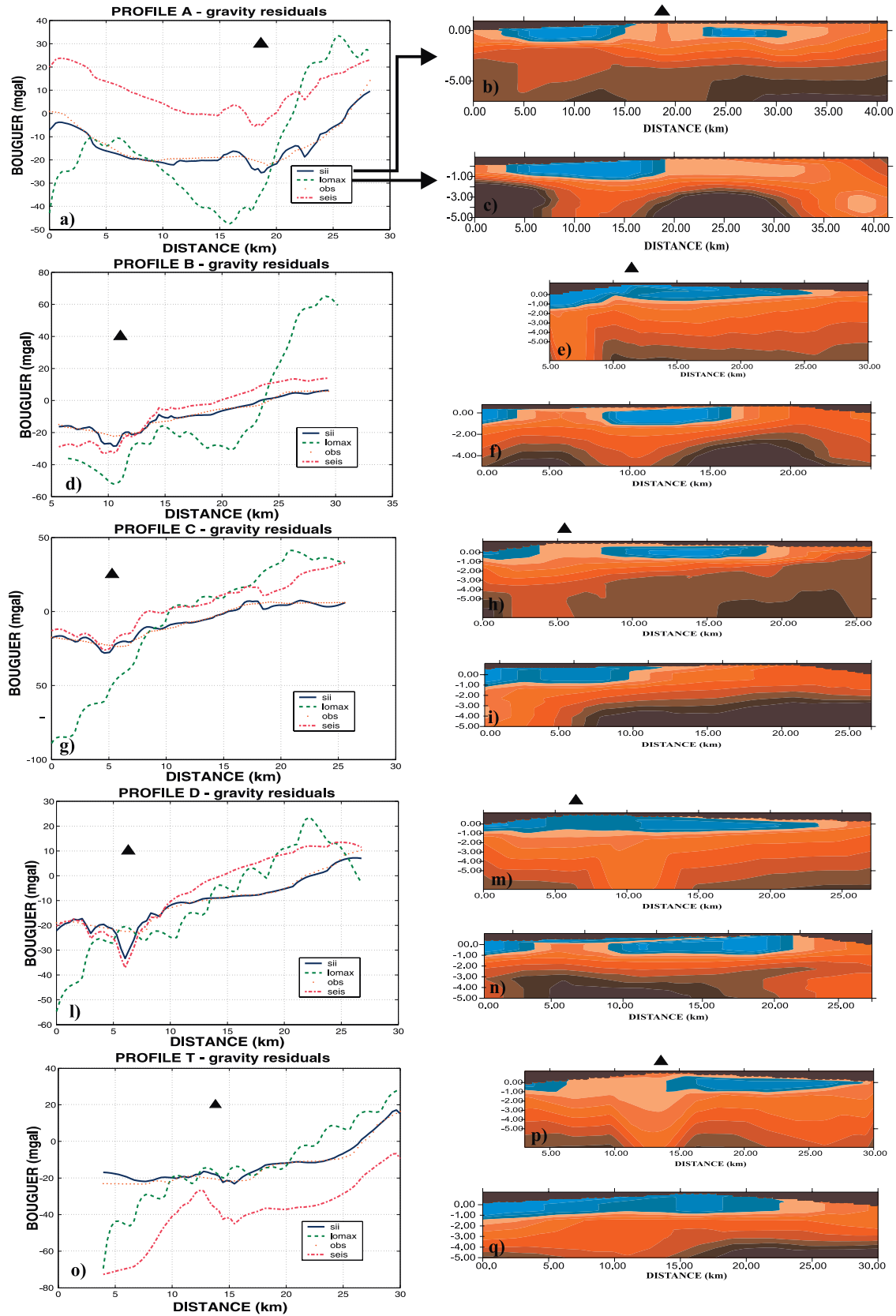
Figure 8. (a, d, g, l, o) Diagrams of the gravity response of final seismic and SII models. For each profile, RMS associated to residuals between observed and SII curves is indicated. Each diagram shows also the response recovered from the models by *Lomax et al.* [2001]. Beside each diagram comparison of density solution for (b, e, h, m, p) SII and (c, f, i, n, q) Lomax models. Position of Mount Vesuvius is indicated by a solid triangle.

Table 3. Comparison of Seismic and SII Recovered Velocities for the Five Profiles[a]

	Node 1	Node 2	Node 3	Node 4	Node 5	Node 6	Node 7	Node 8	Node 9	Node 10	Node 11	Node 12	Node 13
Profile A: Shot Points 0.00/16.304/22.313/40.352 km													
X, km	0.00	3.73	7.45	11.18	14.91	18.64	22.36	26.09	29.82	33.55	37.27	41.00	
Seismic Velocities, km/s													
Topography	3.25	1.70	1.43	1.79	1.46	**1.96**	**1.86**	1.61	2.31	3.16	3.80	3.96	
Second boundary	3.39	2.13	2.11	2.72	2.62	**3.17**	2.41	2.03	2.66	3.40	3.97	4.14	
Third boundary	5.00	5.40	5.35	3.76	3.37	**4.07**	3.58	3.63	3.87	4.12	4.26	4.32	
Fourth boundary	6.10	6.58	6.29	5.53	5.43	5.87	6.50	6.20	6.13	6.04	5.82	5.77	
Bottom	6.67	6.69	6.74	6.80	6.91	6.64	6.81	6.82	6.78	6.75	6.79	6.82	
SII Velocities, km/s													
Topography	3.24	1.69	1.29	1.97	1.74	**2.20**	**1.83**	1.61	2.90	3.17	3.86	3.98	
Second boundary	3.38	2.12	1.97	2.90	2.90	**3.41**	2.38	2.03	3.25	3.41	4.03	4.16	
σ, km/s	0.06	0.078	0.091	0.123	0.073	0.093	0.061	0.108	0.140	0.140	0.128	0.130	
Third boundary	5.03	5.32	5.26	3.84	3.55	**4.21**	3.55	3.57	3.48	3.41	4.03	4.16	
σ, km/s	0.12	0.107	0.133	0.124	0.103	0.095	0.131	0.138	0.140	0.140	0.140	0.140	
Fourth boundary	6.12	6.46	6.23	5.59	5.55	5.89	6.31	6.19	6.44	6.09	5.77	5.78	
σ, km/s	0.13	0.122	0.123	0.116	0.119	0.117	0.123	0.129	0.125	0.124	0.119	0.139	
Bottom	6.72	6.39	6.45	6.75	7.01	6.60	6.60	6.74	6.94	6.94	6.88	6.90	
σ, km/s	0.14	0.140	0.138	0.129	0.134	0.139	0.139	0.138	0.132	0.139	0.140	0.140	
Profile B: Shot Points 30.00/19.374/8.845 km													
X, km	5.00	5.89	7.72	10.08	11.07	12.10	13.93	15.61	19.23	23.00	25.98	27.65	30.00
Seismic Velocities, km/s													
Topography	1.75	1.67	1.51	1.89	2.14	2.18	2.15	1.96	1.91	2.17	2.43	2.64	2.77
Second boundary	2.21	2.07	1.91	2.54	2.90	2.76	2.65	2.29	2.27	2.85	3.67	4.11	4.23
Third boundary	3.79	3.82	3.94	3.90	4.07	4.02	3.98	3.90	3.94	4.04	4.20	4.40	4.26
Bottom	6.31	6.33	6.33	6.44	6.08	6.39	6.74	5.89	6.14	6.15	6.49	6.08	6.66
SII Velocities, km/s													
Topography	1.87	1.74	1.56	1.56	2.28	2.19	2.25	1.86	1.77	2.19	2.52	2.74	2.84
Second boundary	2.33	2.14	1.96	1.96	**3.04**	2.77	2.75	2.19	2.13	2.87	3.76	4.21	4.30
σ, km/s	0.17	0.157	0.0603	0.1406	0.1050	0.1064	0.1311	0.1413	0.0830	0.1534	0.1687	0.1681	0.1525
Third boundary	4.08	3.91	4.17	**4.53**	**4.50**	4.13	3.89	3.76	3.89	4.28	4.19	4.46	4.27
σ, km/s	0.170	0.168	0.1306	0.1360	0.1559	0.1523	0.1586	0.1369	0.1447	0.1322	0.1689	0.170	0.169
Bottom	7.45	6.83	7.29	7.31	6.69	6.87	6.74	6.05	6.71	6.18	6.52	6.49	7.04
σ, km/s	0.170	0.170	0.169	0.168	0.168	0.162	0.163	0.157	0.154	0.152	0.158	0.160	0.168
Profile C: Shot Points 26.000/18.750/8.539/2.923 km													
X, km	0.00	2.36	4.73	7.09	9.45	11.82	14.18	16.55	18.91	21.27	23.64	26.00	
Seismic Velocities, km/s													
Topography	2.06	2.32	2.33	2.26	1.30	1.80	1.88	2.14	2.70	3.44	3.63	4.14	
Second boundary	2.36	2.81	3.21	2.64	2.20	2.27	2.26	2.37	3.14	4.00	3.83	4.36	
Third boundary	3.85	3.82	3.83	4.05	4.12	4.07	3.78	3.58	4.16	4.95	4.94	5.10	
Fourth boundary	5.64	5.61	5.58	5.71	5.65	5.73	5.70	5.67	5.88	5.65	5.64	5.72	
Bottom	6.49	6.50	6.51	6.53	6.49	6.47	6.46	6.47	6.51	6.51	6.50	6.51	
SII Velocities, km/s													
Topography	2.09	2.44	**3.21**	**2.64**	1.81	1.67	1.62	2.29	2.94	3.80	3.63	4.34	
Second boundary	2.39	2.93	**4.09**	**3.02**	2.03	1.90	1.80	2.52	3.38	4.36	3.83	4.56	
σ, km/s	0.1528	0.0611	0.1213	0.1270	0.0231	0.1561	0.1544	0.1497	0.1299	0.1500	0.1594	0.1547	
Third boundary	3.95	4.27	4.59	4.04	4.08	4.42	3.66	3.10	4.50	5.46	5.29	5.26	
σ, km/s	0.1590	0.1516	0.1507	0.1503	0.1396	0.1425	0.1460	0.1242	0.1379	0.1413	0.1369	0.1572	
Fourth boundary	5.97	6.08	6.17	5.83	5.40	5.67	5.68	5.52	5.89	5.58	5.50	5.73	
σ, km/s	0.1600	0.1600	0.1569	0.1530	0.1519	0.1480	0.1469	0.1484	0.1518	0.1492	0.1468	0.1591	
Bottom	7.09	6.89	6.90	6.73	6.52	6.58	6.58	6.26	7.05	6.88	5.16	6.51	
σ, km/s	0.1600	0.1600	0.1600	0.1600	0.1589	0.1563	0.1550	0.1550	0.1548	0.1549	0.1595	0.1600	
Profile D: Shot Points 27.000/18.520/2.747 km													
	Node 1	Node 2	Node 3	Node 4	Node 5	Node 6	Node 7	Node 8	Node 9	Node 10			
X, km	0.00	3.00	6.00	9.00	12.00	15.00	18.00	21.00	24.00	27.00			
Seismic Velocities, km/s													
Topography	1.27	1.77	2.47	1.41	1.30	1.18	1.31	2.05	2.97	3.99			
Second boundary	1.85	2.69	2.87	2.65	2.87	2.97	3.03	2.95	3.80	4.39			
Third boundary	3.67	3.57	3.81	3.95	4.21	4.22	4.16	4.18	4.36	4.40			
Bottom	6.30	6.28	6.31	6.46	6.43	6.54	6.55	6.67	6.71	6.42			

Table 3. (continued)

	Node 1	Node 2	Node 3	Node 4	Node 5	Node 6	Node 7	Node 8	Node 9	Node 10	Node 11
Profile D: Shot Points 27.000/18.520/2.747 km											
SII Velocities, km/s											
Topography	1.24	1.86	2.80	1.54	1.25	1.20	1.29	2.01	2.96	3.98	
Second boundary	1.82	2.78	3.20	2.78	2.82	2.99	3.01	2.91	3.79	4.38	
σ, km/s	0.1401	0.0659	0.0889	0.0881	0.1335	0.1368	0.0949	0.1528	0.1468	0.1448	
Third boundary	3.48	3.58	4.05	3.96	4.11	4.22	4.10	4.13	4.35	4.39	
σ, km/s	0.1705	0.1323	0.1378	0.1539	0.1511	0.1325	0.1482	0.1336	0.1442	0.1761	
Bottom	6.20	6.47	6.72	6.56	6.21	6.34	6.16	6.30	6.56	6.45	
σ, km/s	0.18	0.1722	0.1546	0.1564	0.1567	0.1537	0.1657	0.1545	0.1489	0.1782	
Profile T: Shot Points 29.990/16.916/10.959 km											
X, km	3.06	6.75	9.77	12.53	13.80	16.08	18.44	21.80	26.37	29.32	30.00
Seismic Velocities, km/s											
Topography	1.68	1.65	**1.86**	**1.98**	**2.11**	1.55	1.72	1.73	1.70	3.47	3.61
Second boundary	1.85	1.76	1.89	**2.52**	**2.57**	2.38	2.17	2.23	2.20	4.03	4.11
Third boundary	2.88	2.80	2.59	4.02	3.89	3.95	3.82	3.75	3.34	4.29	4.30
Bottom	4.98	5.08	5.19	6.02	6.04	6.10	6.10	6.06	6.19	6.12	6.00
SII Velocities, km/s											
Topography	2.11	2.55	2.20	1.90	**2.49**	1.55	1.79	2.06	1.76	3.40	3.66
Second boundary	2.28	2.66	2.23	**4.09**	**2.95**	2.38	2.24	2.56	2.26	3.96	4.16
σ, km/s	0.1793	0.1752	0.0858	0.1552	0.1182	0.0487	0.0435	0.1458	0.1714	0.1713	0.1773
Third boundary	3.36	3.51	2.58	3.42	3.90	4.27	4.07	4.08	3.20	4.29	4.32
σ, km/s	0.1797	0.1481	0.1241	0.1292	0.1432	0.1554	0.1553	0.1530	0.1647	0.1799	0.1800
Bottom	7.02	6.93	5.93	5.85	6.31	6.98	7.55	7.18	7.06	6.59	7.01
σ, km/s	0.1800	0.1800	0.1799	0.1774	0.1715	0.1683	0.1618	0.1358	0.1468	0.1712	0.1800

[a]For each boundary, seismic and SII velocities and the SD error (σ) are given for the specified distance. Velocity values related to the shallow high-velocity body are indicated in bold.

the interface representing the topography. In order to prevent edge effects during interpolation, the model is boxed into a $35 \times 55 \times 10$ km parallelepiped. The irregular velocity grid is created through the use of tricubic B splines and a smoothing algorithm useful to design optimum models for asymptotic ray theory methods.

[28] In nonsmoothed models, the behavior of rays becomes chaotic and as a consequence geometrical spreading and the number of arrivals increase rapidly with travel time [*Smith et al.*, 1992; *Abdullaev*, 1993; *Tappert and Tang*, 1996; *Witte et al.*, 1996; *Keers et al.*, 1997]. Therefore it is necessary to prepare models which are (1) not far from the real one and (2) sufficiently smooth for ray tracing. The smoothing algorithm we have decided to use, allows the quantification of the exponential divergence of rays in terms of a physical quantity: the exponent of Lyapunov [*Lyapunov*, 1949; *Klimeš*, 2002]. Since the Lyapunov exponent depends on the second spatial derivatives of the velocity or slowness, and the exponent grows as the divergence increases, the key issue is to build up a model by minimizing the second derivatives of the functions representing the model parameters. The minimization of velocity is therefore developed inside the Sobolev space H^2. By definition, H^2 is the space of L_2 functions, whose partial derivatives up to order 2 are L_2 functions. The minimization of the Sobolev norm of slowness yields to the resolving formula [*Žáček*, 2002]:

$$\mathbf{u} = \left[\mathbf{B}^{\mathrm{T}}\mathbf{C}^{-1}\mathbf{B} + s^2\,\mathbf{D}\right]^{-1}\mathbf{B}^{\mathrm{T}}\mathbf{C}^{-1}\mathbf{u}^{\mathrm{D}}, \qquad (3)$$

where $\mathbf{B}$ is the matrix of the coefficients of the Sobolev scalar product, $\mathbf{C}$ is a diagonal weighting matrix with elements equal to N (number of grid points), $\mathbf{D}$ is the matrix of the second partial derivatives, s is a parameter depending on the average Lyapunov exponent of the model ($s \sim \hat{\lambda}^{-2}$, see equation 51 of *Klimeš* [2002] and equation 18 of *Žáček* [2002]), and $\mathbf{u}^{\mathrm{D}}$ is the value of slowness in the starting model.

[29] In order to produce a model suitable for ray tracing, a smoothing is also performed on the interface representing the topography. The estimated RMS between the starting and final surface defined in a regular grid of 26×46 cells of 1×1 m, is 0.008188442 km. Several velocity grids have been tested and one with an acceptable Lyapunov exponent and the minimum difference with the starting models is chosen. Our final 3-D model obtained from the interpolation of seismic models, is gridded with $13 \times 24 \times 14$ cells and the calculated RMS difference of slowness is 0.2492 s/km, corresponding to an average RMS between the starting and final velocity model of 0.015 km/s. Using the same grid and the same value of the weighting parameter s ($s = 4$) the RMS difference of slowness for the models recovered by SII is 0.2128927 s/km. As $s \sim \hat{\lambda}^{-2}$ and $e^{\lambda \tau \mathrm{MAX}}$ is roughly proportional to the number of arrivals expected at each point of the model [*Klimeš*, 2000, 2002], we expect a maximum of 12 arrivals.

[30] We assess the quality of the 3-D interpolated velocity model by examining the consistency between the observed and calculated travel times for the in-profile shot gathers (shots and stations on the same profile) and fan shot gathers (shots on a profile and recording stations on a crossing one) (Figures 9, 10, 11, 12, and 13). The arrival times through the medium are calculated using the 3-D numerical ray tracing package CRT5 developed by the Consortium For Seismic
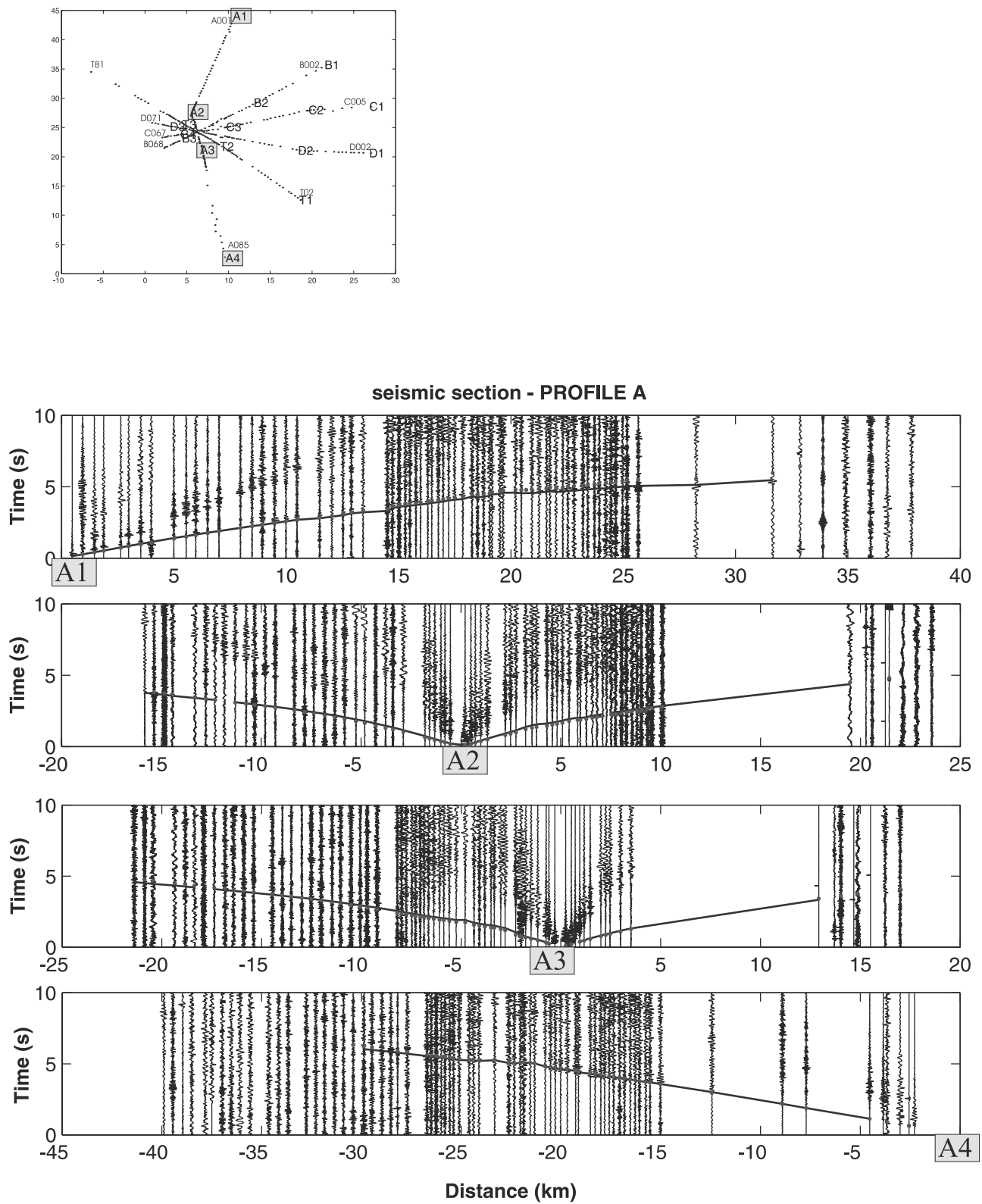
Figure 9. Seismic sections along profile A with indicated the corresponding predicted first arriving *P* times from the 3-D seismic and SII models (dots correspond to SII model and solid line corresponds to seismic model). (top) Study area showing the five profiles (A, B, C, D, T) and shot points. Gray squares indicate the in-profile shots points.
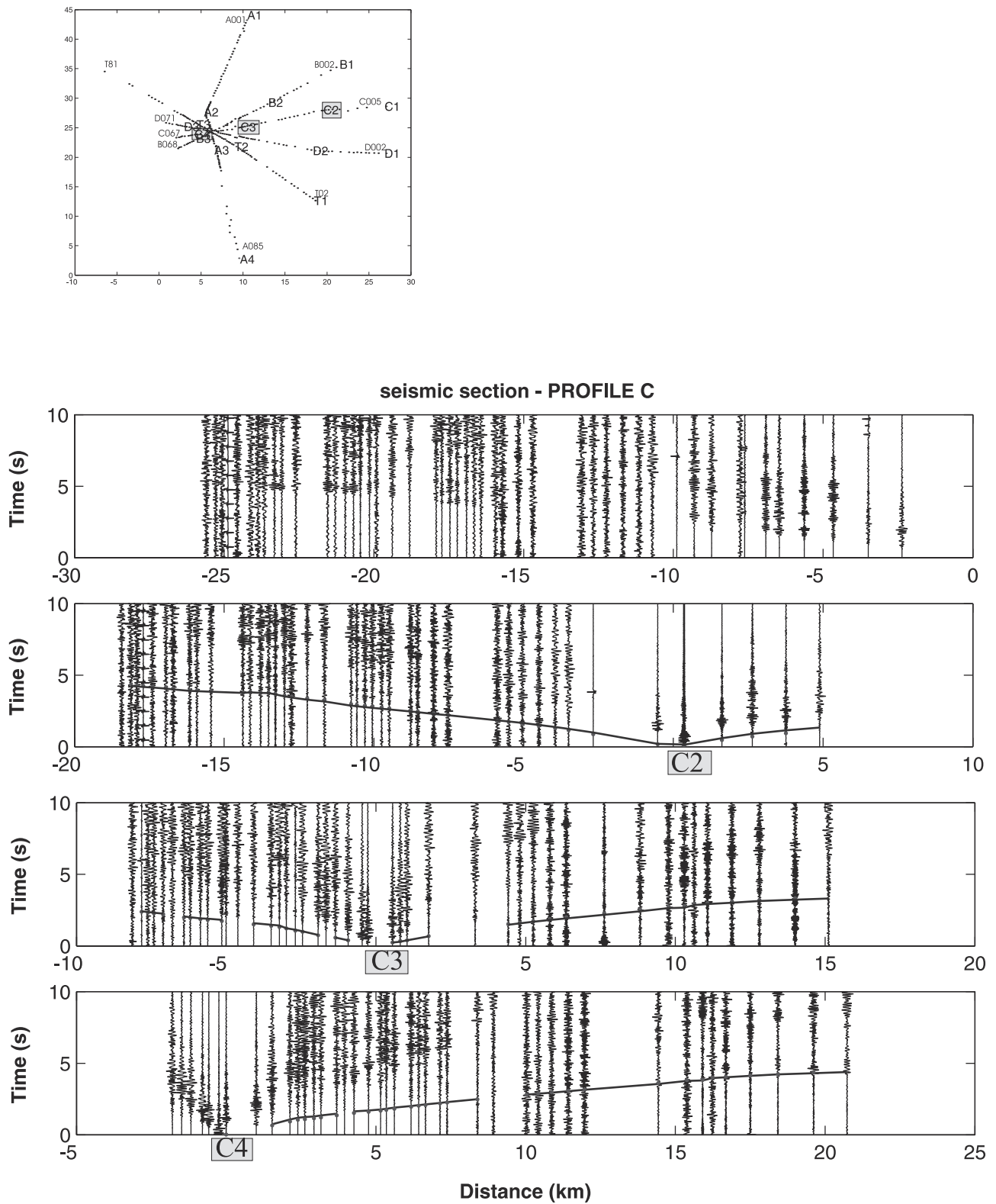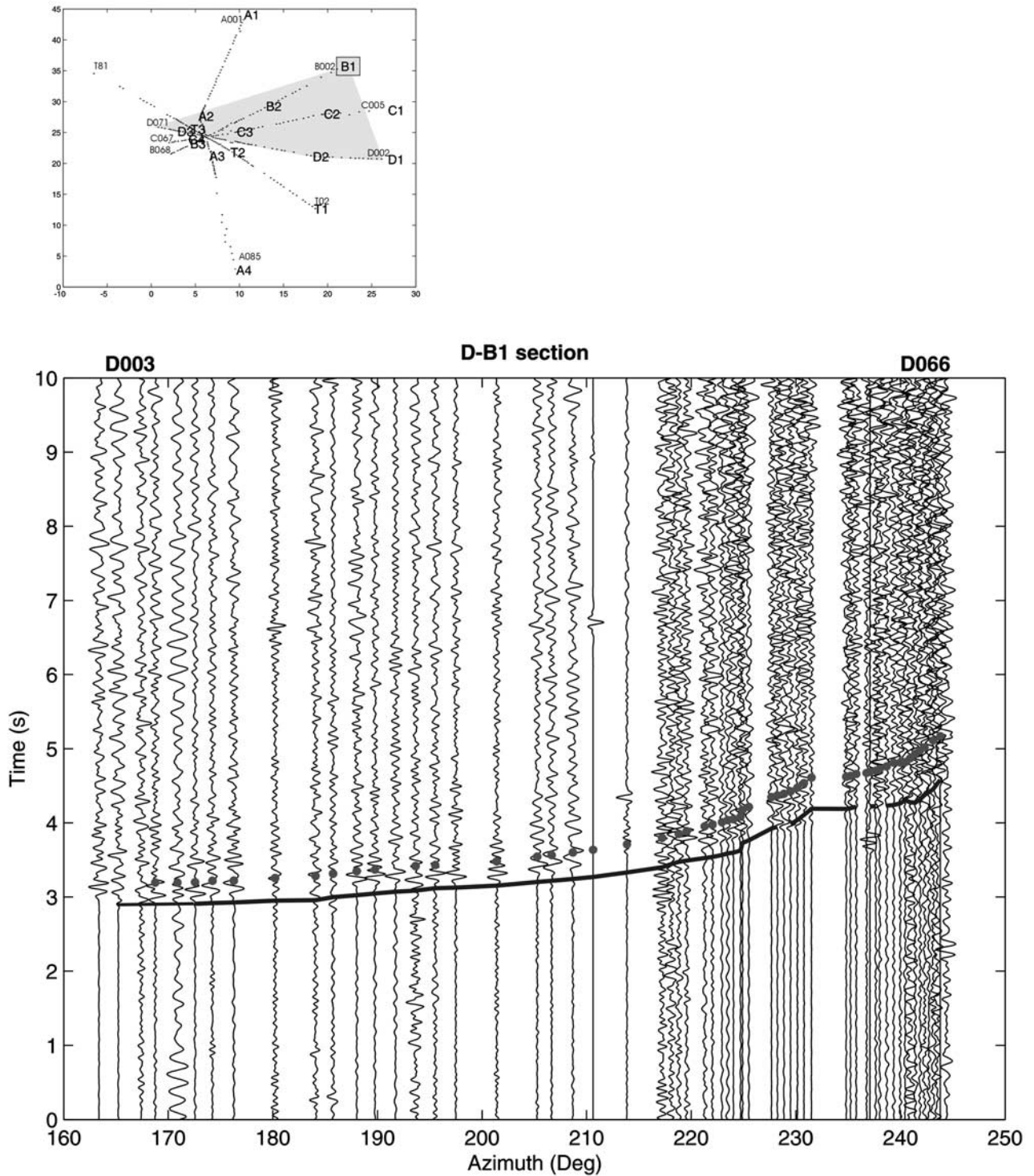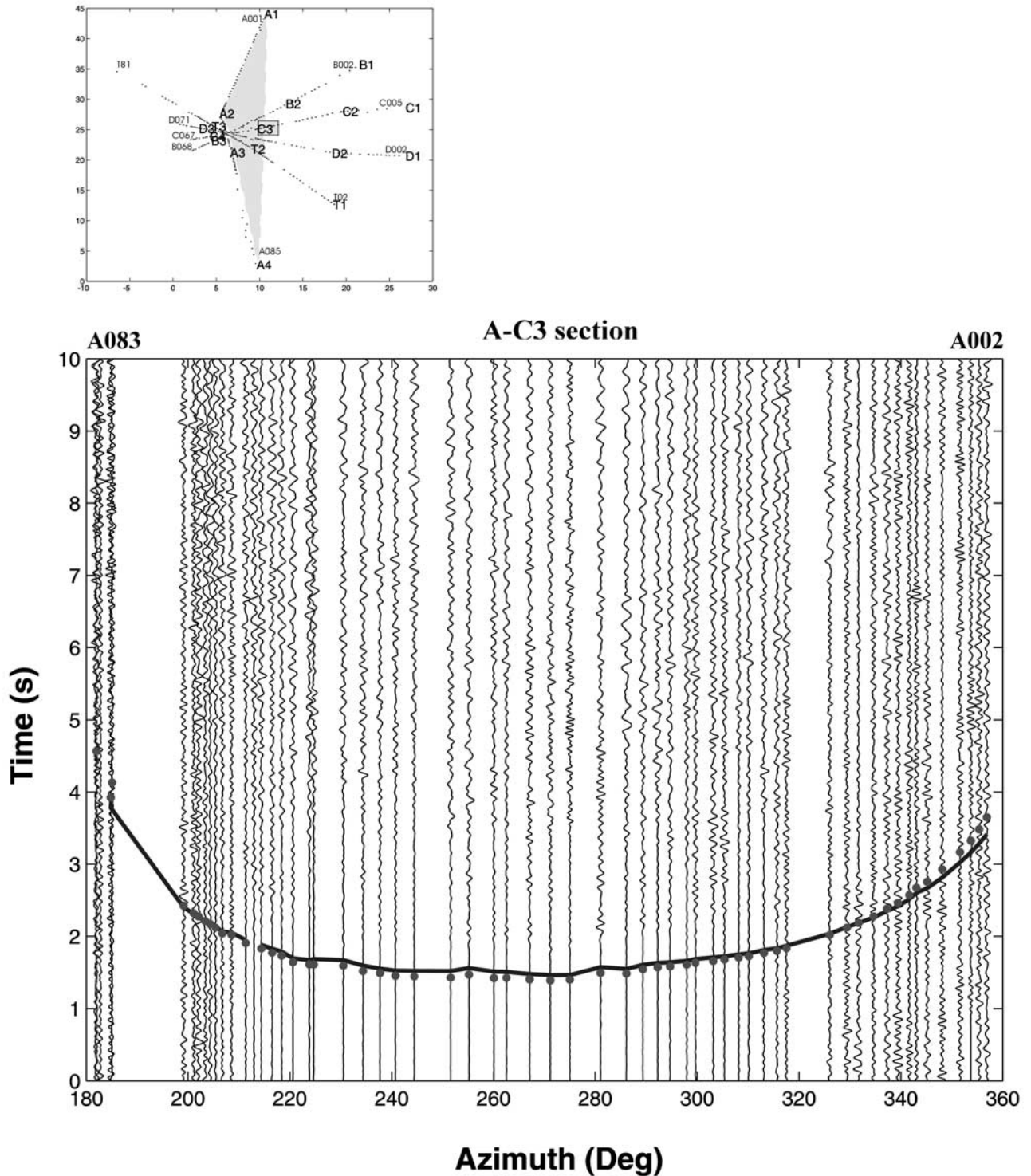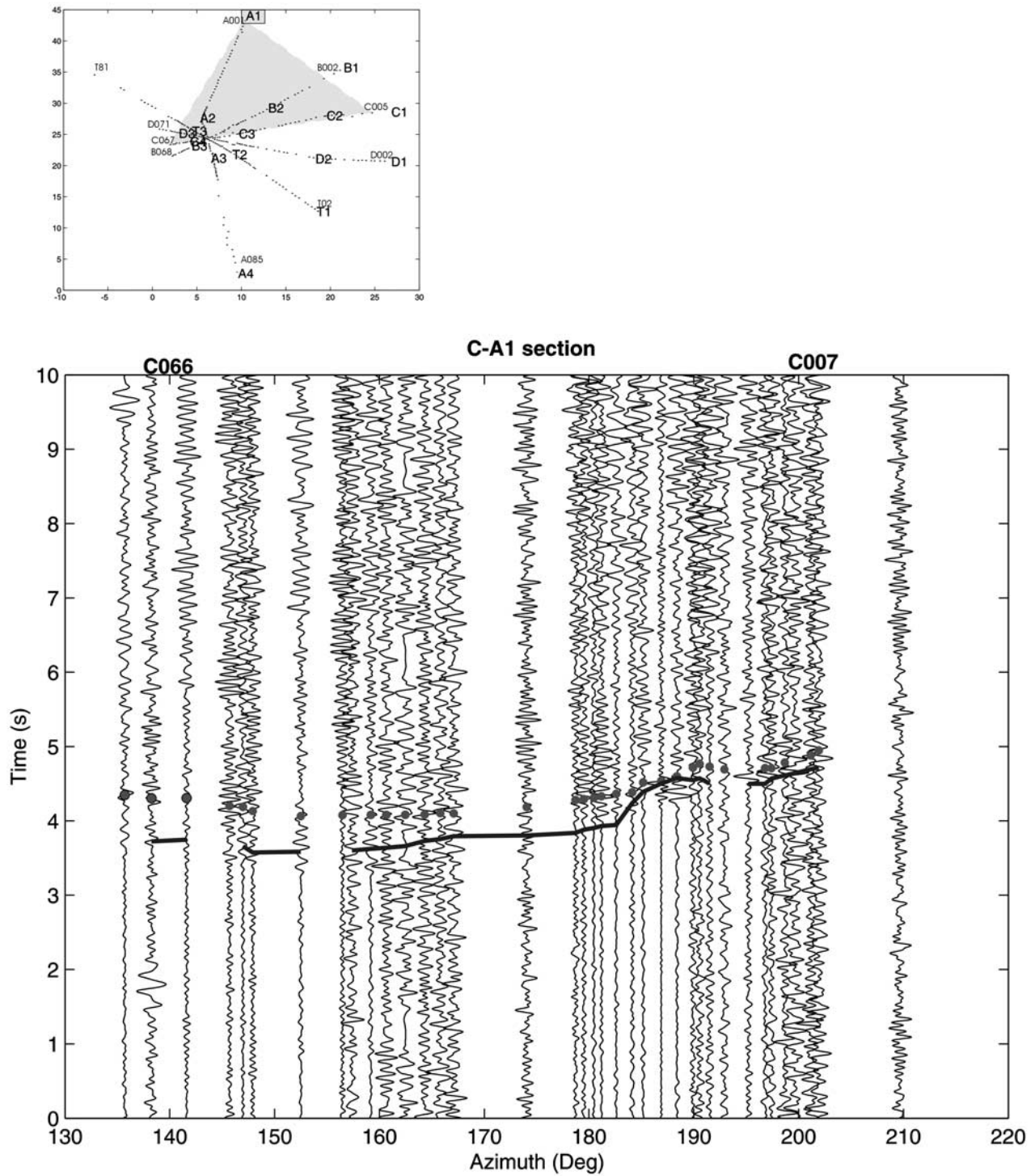
Figure 10. Seismic sections along profile C with indicated the corresponding predicted first arriving *P* times from the 3-D seismic and SII models (dots line corresponds to SII model and solid line corresponds to seismic model). (top) Study area showing the five profiles (A, B, C, D, T) and shot points. Gray squares indicate the in-profile shots points.

Figure 11.   Seismic section for fan profile B1-D with indicated the corresponding predicted first arriving *P* times from the 3-D seismic and SII models (dots correspond to SII model and solid line corresponds to seismic model). (top) Study area showing the five profiles (A, B, C, D, T) and shot points. Gray shading indicates the area crossed by seismic rays.

Waves in Complex 3-D Structures (CW3D) at Charles University, in Prague [Červený et al., 1988; Bulant, 1996].

[31]   As only the in-profile shot data are used to construct the 2-D sections and consequently the interpolated 3-D model, the comparison between the observed and predicted in-profile arrival time curves is a check on the reliability of the interpolation algorithm, while the comparison between fan arrival time curves assesses the goodness of the new 3-D

Figure 12. Seismic section for fan profile C3-A with indicated the corresponding predicted first arriving *P* times from the 3-D seismic and SII models (dots correspond to SII model and solid line corresponds to seismic model). (top) Study area shows the five profiles (A, B, C, D, T) and shot points. Gray shading indicates the area crossed by seismic rays.

model. Most of the calculated times fall within the uncertainty range of the observed times (Figure 14), with a calculated mean error of 0.12 (±0.012) s for the seismic model and of 0.10 (±0.011) s for the SII model. The mean

error shows a slight overestimate of velocity in both models and no significant deterioration of the results with the SII model. The most important mismatch, in terms of delayed travel times, is found for arrivals related to shot

Figure 13. Seismic section for fan profile A1-C with indicated the corresponding predicted first arriving *P* times from the 3-D seismic and SII models (dots correspond to SII model and solid line corresponds to seismic model). (top) Study area showing the five profiles (A, B, C, D, T) and shot points. Gray shading indicates the area crossed by seismic rays.

A1, B1 (only for the SII model, see Figures 11 and 13), D2, and T1.

[32] We explain this difference, by the effect of interpolation of velocities that reduces high velocities of the carbonate outcrops structure. The predicted arrival times are systematically lower for the fan shot gathers which illuminate the central part of the model, under the Gran Cono, especially in the SII model (Figure 12). This could be
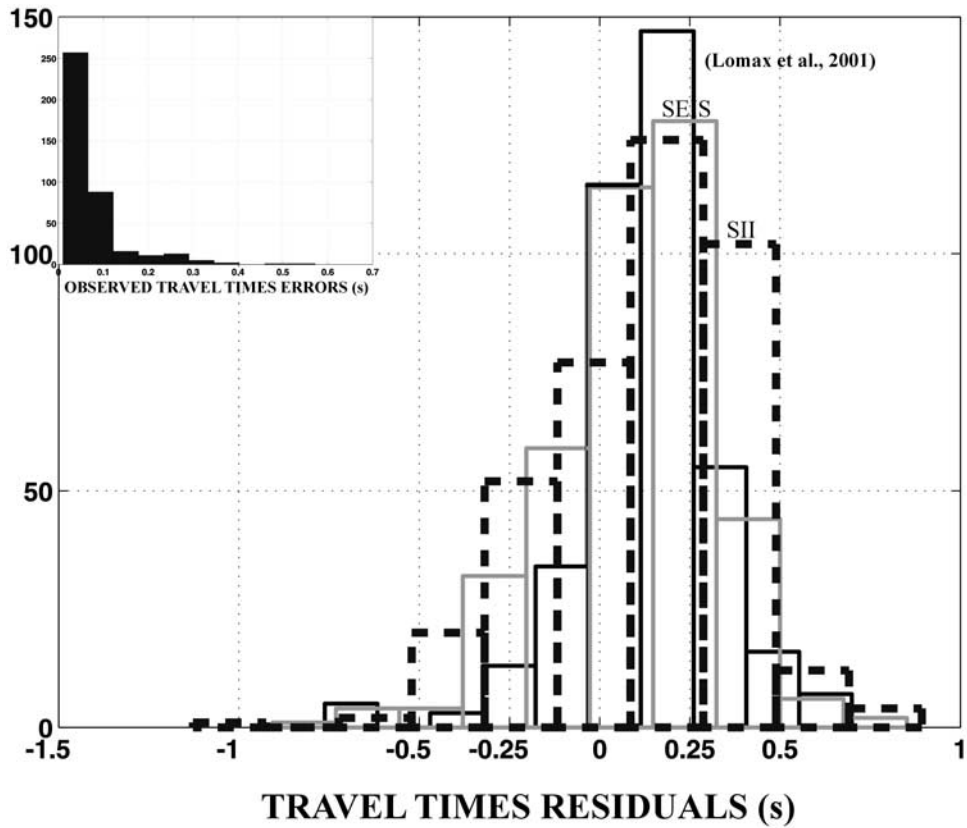
Figure 14. Histograms of residuals between observed and calculated travel times for Lomax et al. (solid black line), seismic (solid grey line), and SII (dashed line) models. Inset is a histogram of the observed travel time errors.
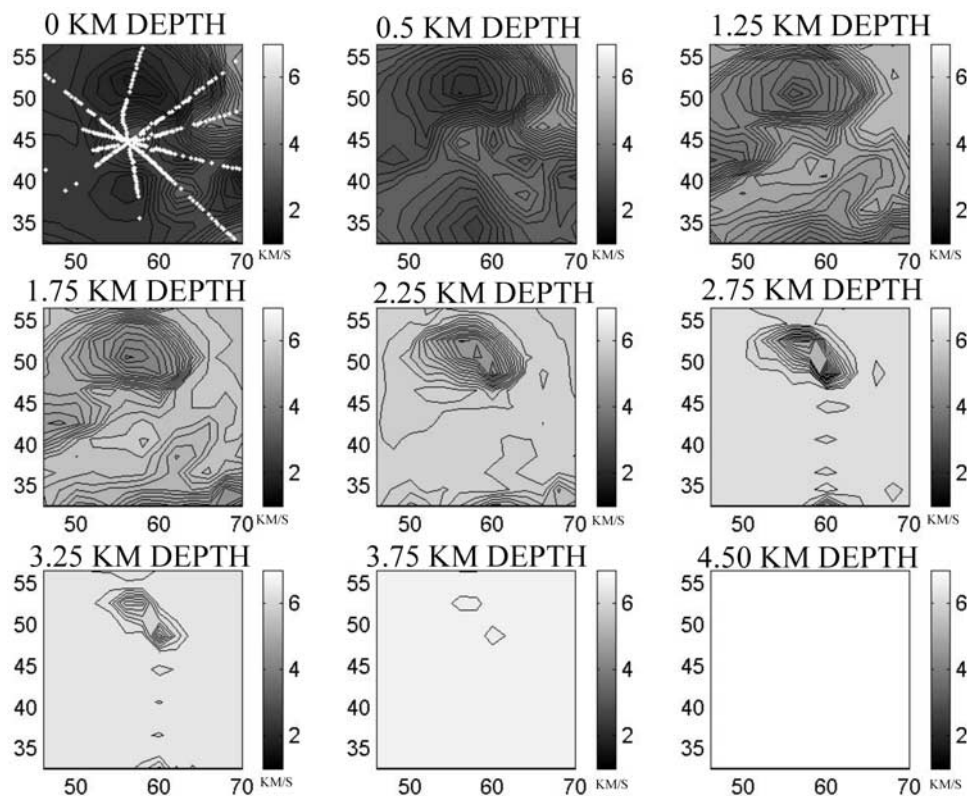
Figure 15. Horizontal sections of the *Lomax et al.* [2001] 3-D velocity model. Velocity is contoured at 0.12 km/s intervals. The five profiles of TOMOVES experiment are superimposed on the first section.
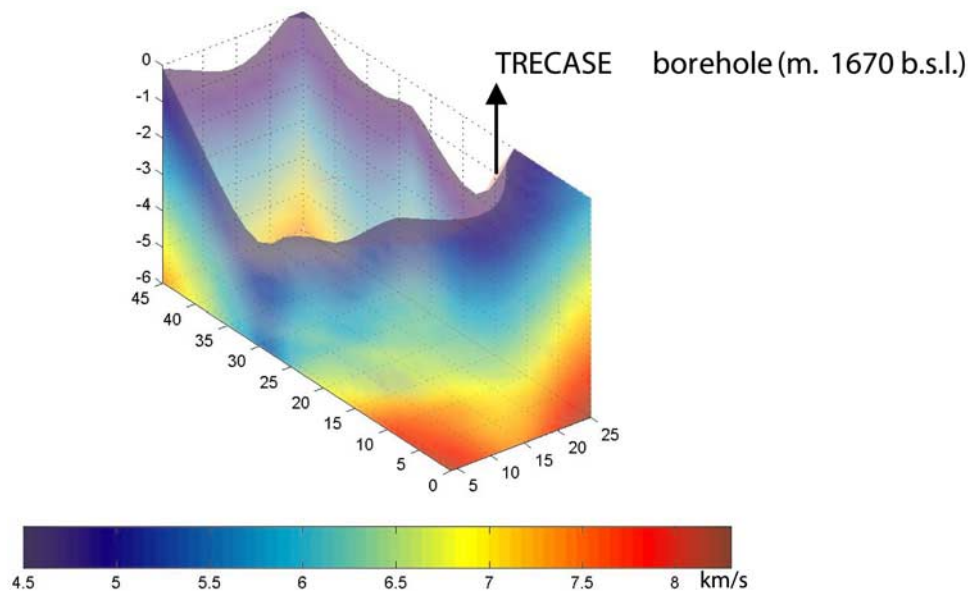
Figure 16. Assumed top of carbonate basement, as recovered from interpolated 3-D SII model. The arrow indicates position of TRECASE borehole measurement.

due or to a general overestimate in velocity under the volcano or to the presence of the high-velocity body, detected by 2-D modeling and which can be one of the results of the deviation of the shot-receiver geometry from a line. A quantitative comparison between the travel times produced by our models and the 3-D model developed by *Lomax et al.* [2001] (Figure 14) shows similar trends and residuals (a mean of 0.13 ± 0.009 s).

[33] Hence we may conclude that the interpolated SII 3-D model is consistent with the observed *P* first arrival times. In fact, the mean discrepancies between calculated and observed travel times are in the range of the estimated picking errors for the in-profile and fan shot gathers (Figure 14), which have a mean error of 0.067 s. The model provides an initial reference model for a complete 3-D tomographic inversion of seismic data and 3-D gravity modeling is straightforward.

4. Results and Conclusions

[34] Once we have built the 3-D velocity model of Mount Vesuvius and the surrounding area, we want to compare our results with previous geophysical studies. The purpose of comparing the general features of the retrieved model is twofold. First, the comparisons serve as a check on the validity of our inversion technique. Second, since the interpretation of seismic velocities in terms of medium properties is a complicated task, because of the large number of variables involved, the comparisons provide a more realistic estimate of the computed model parameters.

[35] The prominent features evidenced by our 2-D SII velocity models are (1) a sharp velocity variation (from 1.5–2.5 km/s to 4–6 km/s) between the shallowest layer and the deeper structures at depths (0.5 to 1.8 km) corresponding to the discontinuity between the alluvial/volcanic sediments and the carbonatic substratum; (2) a shallow high-velocity body under the volcano, percentage positive

anomaly being in the order of 1–2%, between 15 and 21 km in profile A, between 8 and 13 km in profile B, between 3 and 7 km in profile C, between 10 and 15 km in profile T (Figure 7 and Table 3); and (3) a low-velocity region in the SE side of profile T and E side of profile D. The density models (Figure 8) are consistent with the velocity models but show a more pronounced relative low-density region in profile B and C and between 8 and 12 km in profile D, at depths greater than 3 km.

[36] The contribution of gravity data enhances the reconstruction of the three main structural features and combines information which was given separately from previous gravity and seismic modeling. This is clearly visible if we compare the 3-D model reconstructed by *Lomax et al.* [2001] with our 3-D SII interpolated model. Horizontal sections of the imaged volume by *Lomax et al.* (Figure 15) well resolve a 8-km-wide depression to the north of Vesuvius, but little evidence is given for the high-velocity body below the volcano and for the low-velocity region SE of Mount Vesuvius.

[37] Furthermore, due to poor or absent seismic resolution down to 3 km, only the shallowest top of the carbonate basement is sampled and we do not have any information about the connection of shallow structures to deeper structures. Our 3-D SII model provides information up to 6 km depth and thus we can clearly recover the continuity of the Mesozoic carbonate basement under the volcano edifice. This structure is made clear by contouring only velocities higher than 5 km/s (Figure 16).

[38] The basement top depth is consistent with the Trecase well profile. The basement dips gently from the edges of the Campanian Plain toward the volcano edifice and reaches its minimum at a depth of 3.5 km, between 25–35 km in the *y* direction and 5–14 km in the *x* direction, below the NNE flank of Mount Vesuvius. The depression is also clearly visible in the SII 2-D model T, between 7 and 15 km, and in model A, between 7 and 12 km. Hence what we observe
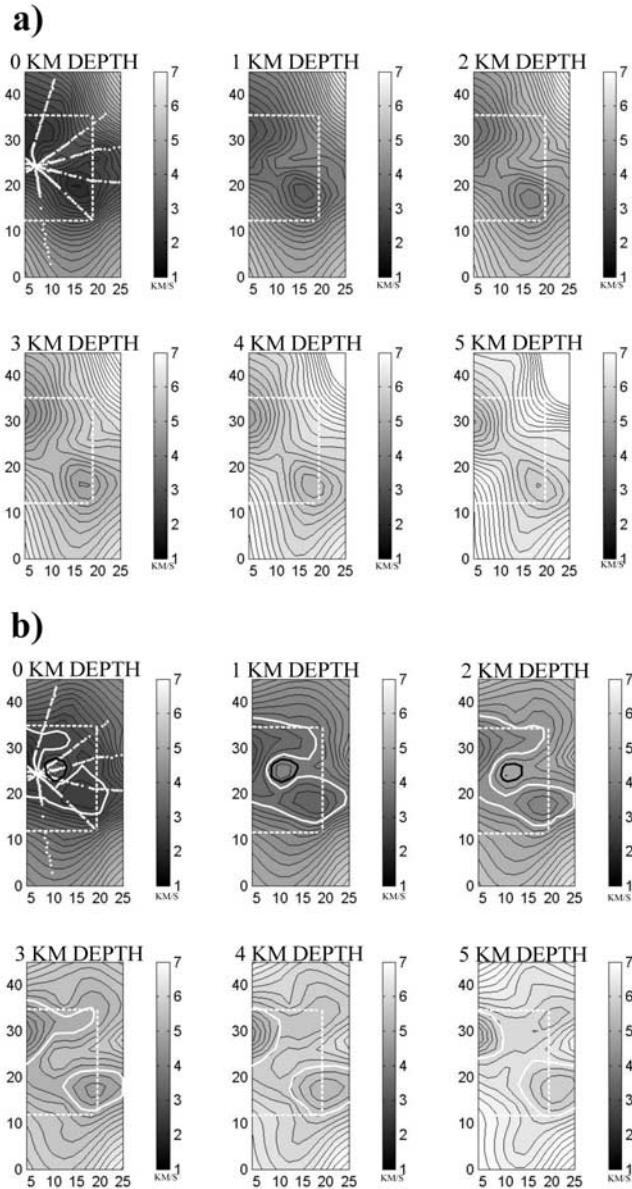
Figure 17. Horizontal sections of (a) seismic and (b) SII 3-D velocity model as indicated by the white dashed line outlining the area studied by *Lomax et al.* [2001]. Velocity is contoured at 0.12 km/s intervals. The five profiles of TOMOVES experiment are superimposed on the first section. Position of the high-velocity body is contoured in black, and the regions with negative percentage velocity anomaly are contoured in white.

from horizontal sections through the imaged velocity volume (Figure 17) is a continuous amphitheater-like depression which extends from the NNW flank of Mount Vesuvius to the eastern flank, reaches its minimum below the sea, turns toward the southeastern flank of the volcano and ends into a SE depression, where previous seismic reflection lines [*Bruno and Rapolla*, 1999] observed NW-SE Quaternary faults. Results of this experiment also showed a rupture surface, associated with an old lateral collapse, that involves the southwestern side of Mount Vesuvius.

[39] In order to image the connection of this anomalous low-velocity structure to deeper magma chambers and feeding sources, we compute the negative percentage velocity anomaly for the SII model in absolute value higher than 2%. We calculate this anomaly for each of the 14 x-y sections, 0.5 km thick:

$$\text{pva}_i = [(v_i - v_m - SD)/(v_m - SD)] \times 100 \quad i = x_i \times y \quad (4)$$

where pva_i is the percentage velocity anomaly, v_i is the velocity node, vm is the mean of each velocity section, and SD is the standard deviation of the mean. A perspective view of the results is shown in Figure 18. In it we may observe a conduit structure, 5 km wide, which extends from the surface to the maximum depth of the model, located in the WNW flank of the volcano, where the Mesozoic carbonate basement reaches its minimum. Hence an important result of this study is that this structure, embedded in the carbonate basement, at shallow depths is conceivably connected to the northern and southeastern depressions, which in terms of hazard prevention, are the regions through which magma may more easily flow toward the surface and cause possible eruptions. The result shows up in this way the close relation between regions of structural weakness of the Mesozoic carbonate basement and future eruptions. Previous studies provide a justification to this evidence. In fact the origin of the volcano is ascribed to the subsidence of the carbonate basement toward the Gulf of Naples [*Fusi*, 1996] caused by an extensive vertical faulting, displaying a parallel (NW-SE) and a normal (NE-SW) trend to the main axis of the Apennines [*Principe et al.*, 1987]. Examples of the influence of the regional tectonics on the feeding system of the volcano are some historic vents (Pollena spattern cone, Colle Umberto cumulo dome, central crater, 1906 vents) which are aligned along the NW-SE system of faults (Figure 19).

[40] The horizontal sections of the imaged SII volume, clearly evidence the anomalous shallow, up to depths of 2 km, high-velocity body, positive percentage velocity anomaly being in the order of 0.5−2%. The position of the body, between 22 and 27 km in the y direction (S-N) and between 8 and 14 km in the x direction (E-W), indicates that it is presumably associated to the shallow earthquakes localized within about 1 km of the Gran Cono crater axis, at depths of about 1 to 3.5 km bsl by *Lomax et al.* [2001] and 2 to 6 km bsl by *De Natale et al.* [1998]. Anyhow, in our opinion the shape of the high-velocity anomaly correlates better with a concentration of cooled magmatic dikes inside the conduit structure, than with a shallow magmatic chamber.

[41] The SII analysis resolves the conduit structure up to 6 km depth. This structure, located NW of Mount Vesuvius (Figures 17 and 18) is conceivably connected to deeper magma chambers and feeding sources. Analysis of wide-angle reflection lines (MAREVES'97 offshore air gun seismic survey) evidences (1) a *P* to *S* conversion at the top of a low-velocity layer at midcrustal depths (about 10 km) which may indicate a magma reservoir [*Auger et al.*, 2001, *Virieux et al.*, 1999] and (2) an upheaval of Moho topography (from 31 km to 26 km depth) below the Phlegraean Fields and the Vesuvius volcanic complex [*de Franco et al.*, 2000], which is explained in terms of a relevant upper mantle−crust volcanological feeding system.
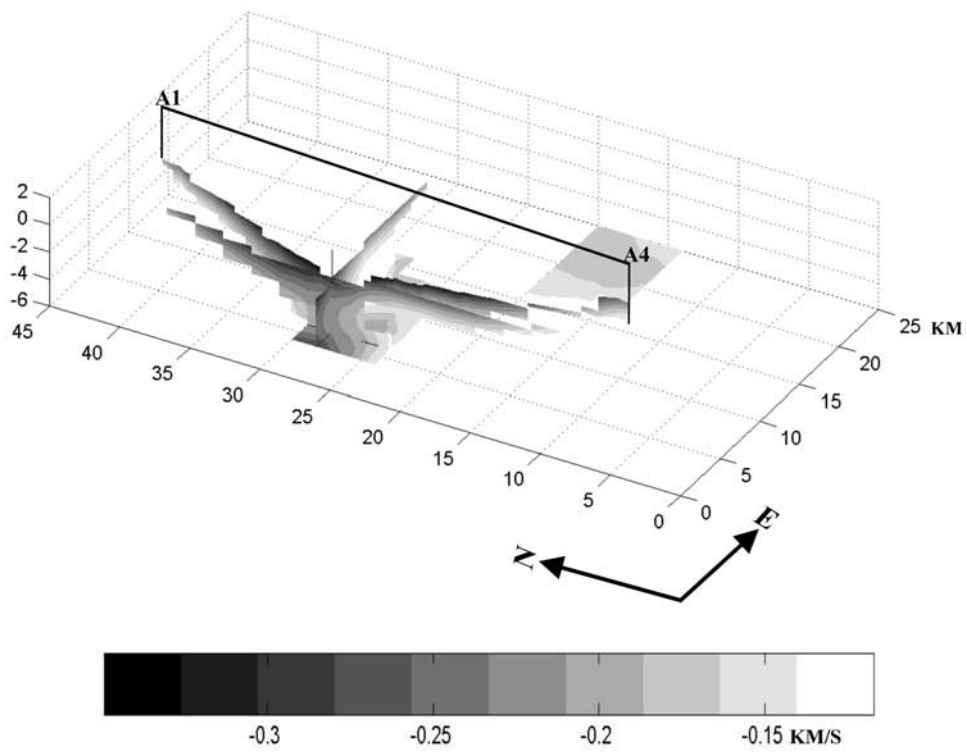
Figure 18. The conduit structure as imaged by two orthogonal vertical sections along profile A from SII 3-D model.
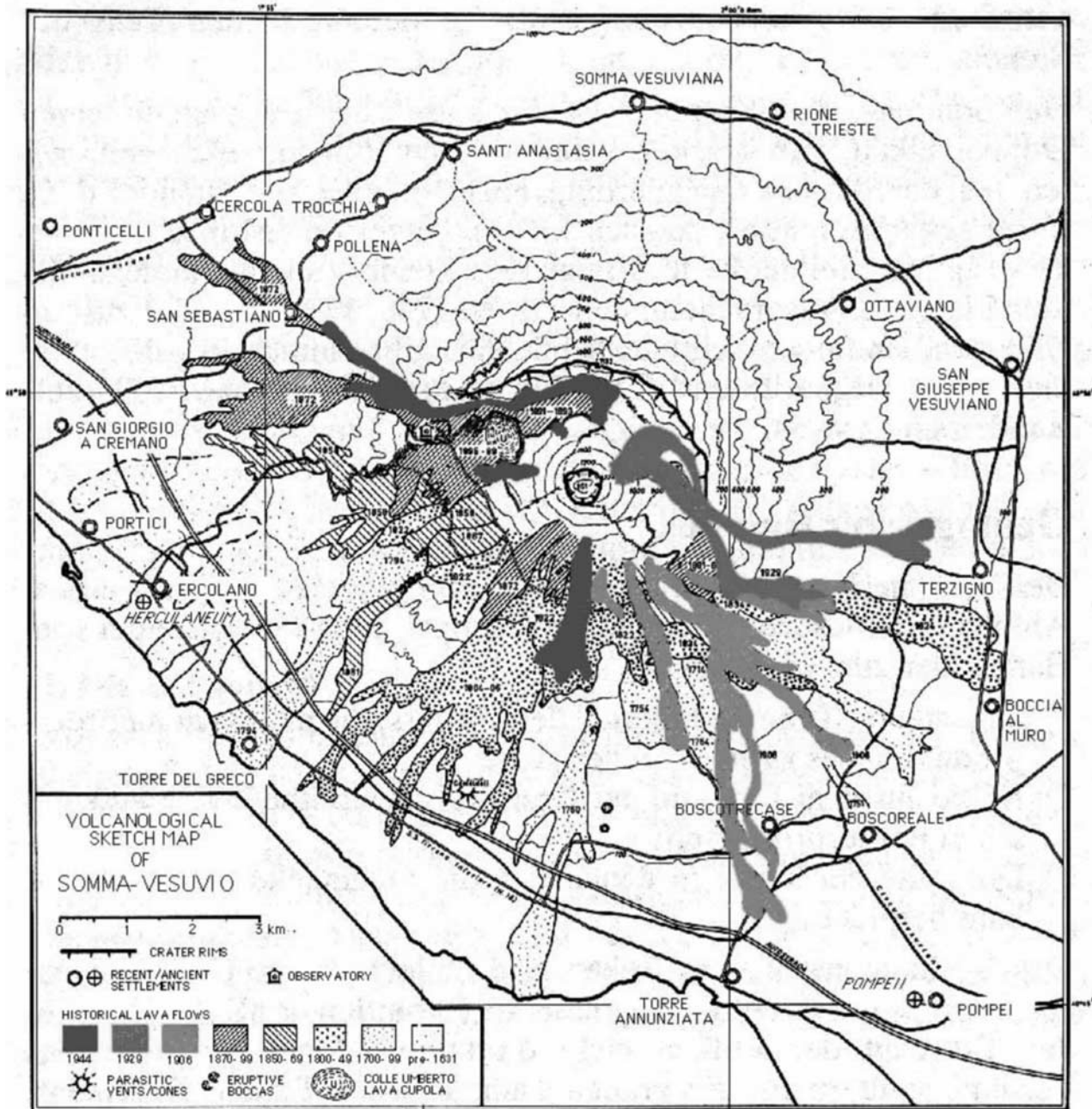
Figure 19. Mount Vesuvius caldera (in Figure 1, the area surrounding the volcano is indicated by dark gray) with indication of historical vents and lava flows.

No significant evidence of the existence of a shallow magma chamber, embedded in the Mesozoic basement [*Rosi et al.*, 1987; *Cortini and Scandone*, 1982] is found.

References

Abdullaev, S. S., *Chaos and Dynamics of Rays in Waveguide Media*, Gordon and Breach, Newark, N. J., 1993.

Auger, E., P. Gasparini, J. Virieux, and A. Zollo, Seismic evidence of an extended magmatic sill under Mt. Vesuvius, *Science*, 294, 1510–1512, 2001.

Barberi, F., M. Rosi, R. Santacroce, and M. F. Sheridan, Volcanic hazard zonation at Vesuvius, in *Forecasting Volcanic Events*, *Dev. Volcanol.*, vol. I, edited by H. Tazieff and J. C. Sabroux, pp. 149–161, Elsevier Sci., New York, 1983.

Barton, P. J., The relationship between seismic velocity and density in the continental crust—A useful constraint?, *Geophys. J. R. Astron. Soc.*, 87, 195–208, 1986.

Barzaghi, R., A. Gandino, F. Sansò, and C. Zenucchini, The collocation approach to the inversion of gravity data, *Geophys. Prospect.*, 40, 451–492, 1992.

Berrino, G., G. Corrado, and U. Riccardi, Sea gravity data in the Gulf of Naples: A contribution to delineating the structural pattern of the Vesuvian area, *J. Volcanol. Geotherm. Res.*, 82, 139–150, 1998.

Bruno, P., and A. Rapolla, Study of the sub-surface structure of Somma-Vesuvius (Italy) by seismic reflection data, *J. Volcanol. Geotherm. Res.*, 92, 373–387, 1999.

Bulant, P., Two-point ray tracing in 3-D, *Pure Appl. Geophys.*, 148, 421–447, 1996.

Bulant, P., Smoothing 2-D model HESS for Kirchhoff migrations, in *Seismic Waves in Complex 3-D Structures*, Rep. 10, pp. 75–82, Charles Univ. Press, Prague, 2000.

Cassano, E., and P. La Torre, Geophysics, in *Somma Vesuvius*, edited by R. Santacroce, *Quad. Ric. Sci.*, 114, 175–196, 1987.

Červený, V., L. Klimeš, and I. Pšenčík, Complete seismic ray-tracing in three-dimensional structures, in *Seismological Algorithms*, D. J. Doornbos, pp. 89–168, Academic, San Diego, Calif., 1988.

Cortini, M. R., and P. Scandone, The feeding system of Vesuvius between 1754 and 1944, *J. Volcanol. Geotherm. Res.*, 12, 393–400, 1982.

de Franco, R., G. Caielli, R. Tondi, G. Biella, and A. Corsi, 1-D and 2-D seismic modelling of TOMOVES 96 data, paper presented at XXIV General Assembly, Eur. Geophys. Soc., The Hague, Netherland, 19–23 April1999.

de Franco, R., G. Caielli, R. Tondi, R. Barzaghi, and G. Biella, and TOMOVES Group, Deep structures in the Vesuvian area (Italy), paper presented at XXV General Assembly, Eur. Geophys. Soc., Nice, France, 25–29 April2000.

De Matteis, R., A. Zollo, and J. Virieux, P-wave arrival time inversion by using the τ-p method: Application to the Mt. Vesuvius Volcano, southern Italy, *Geophys. Res. Lett.*, 24(5), 515–518, 1997.

De Natale, G., P. Capuano, C. Troise, and A. Zollo, Seismicity at Somma-Vesuvius and its implications for the 3D tomography of the volcano, *J. Volcanol. Geotherm. Res.*, 82, 175–197, 1998.

De Vivo, B. D., R. Scandone, and R. Trigila, Mount Vesuvius, special issue, *J. Volcanol. Geotherm. Res.*, 58, 1–387, 1993.

Eberhart-Phillips, D., Three-dimensional velocity structure in northern California Coast Ranges from inversion of local earthquake arrival times, *Bull. Seismol. Soc. Am.*, 76, 1025–1052, 1986.

Eberhart-Phillips, D., and M. Reyners, Continental subduction and three-dimensional crustal structure: The northern South Island, New Zealand, *J. Geophys. Res.*, 102, 11,843–11,861, 1997.

Fedi, M., and A. Rapolla, 3-D inversion of gravity and magnetic data with depth resolution, *Geophysics*, 64, 450–452, 1999.

Fusi, N., Structural settings of the limestone 'basement' and its relationship with the magma uprising in the Gulf of Naples, southern Italy, *Ann. Geofis.*, 39, 493–509, 1996.

Gasparini, P., and TOMOVES Group, Looking inside Mt. Vesuvius, *Eos Trans. AGU*, 79, 229–230, 232, 1998.

Haslinger, F., E. Kissling, J. Ansorge, D. Hatzfeld, E. Papadimitriou, V. Karakostas, K. Makropoulos, H.-G. Kahle, and Y. Peter, 3D crustal structure from local eartquake tomography around the Gulf of Arta (Ionian region, NW Greece), *Tectonophysics*, 304, 201–218, 1999.

Keers, H., F. A. Dahlen, and G. Nolet, Chaotic ray behaviour in regional seismology, *Geophys. J. Int.*, 131, 361–380, 1997.

Kissling, E., S. Husen, and F. Haslinger, Model parametrization in seismic tomography: a choice of consequence for the solution quality, *Phys. Earth Planet. Inter.*, 123, 89–101, 2001.

Klimeš, L., Smoothing the Marmousi model for Gaussian packet migration, in *Seismic Waves in Complex 3-D Structures*, Rep. 10, pp. 63–74, 2000.

Klimeš, L., Lyapunov exponents for 2-D ray tracing without interfaces, *Pure Appl. Geophys.*, 159, 1465–1485, 2002.

Lomax, A., A. Zollo, P. Capuano, and J. Virieux, Precise, absolute earthquake location under Somma-Vesuvius volcano using a new 3D velocity model, *Geophys. J. Int.*, 146, 313–331, 2001.

Luzio, D., D. Miglietta and R. de Franco, Generalizzazione del metodo delle dromocrone ridotte, paper presented at II Convegno, Gruppo Naz. di Geofis. della Terra Solida, Rome, 12–14 Dec.1983.

Lyapunov, A. M., *Problème Général de la Stabilité du Mouvement*, *Ann. Math. Stud.*, vol. 17, Princeton Univ. Press, Princeton, N. J., 1949.

Menke, W., *Geophysical Data Analysis: Discrete Inverse Theory*, Academic, San Diego, Calif., 1984.

Pavlenkova, N. I., Interpretation of refracted waves by the reduced travel time curve method, *Izv. Earth Phys.*, 8, 89–100, 1973.

Principe, C., M. Rosi, R. Santacroce, and A. Sbrana, Explanatory notes to the geological map, in *Somma Vesuvius*, edited by R. Santacroce, *Quad. Ric. Sci.*, 114, 11–51, 1987.

Richter, D., Die Küste von Amalfi. Entdeckung und touristische Konstitution einer europäischen Landschaft, in *Fremdenverkehr und lokale Kultur*, pp. 11–30, KEA, Bremen, Germany, 1996.

Rosi, M., R. Santacroce, and M. F. Sheridan, Volcanic hazard, in *Somma Vesuvius*, edited by R. Santacroce, Quad. Ric. Sci., 114, 197–220, 1987.

Santacroce, R. (Ed.), *Somma-Vesuvius*, Quad. Ric. Sci., 114, 1987.

Scandone, R., L. Giacomelli, and P. Gasparini, Mount Vesuvius: 2000 years of volcanological observations, *J. Volcanol. Geotherm. Res.*, 58, 5–25, 1993.

Smith, K. B., M. G. Brown, and F. D. Tappert, Ray chaos in underwater acoustics, *J. Acoust. Soc. Am.*, 91, 1939–1949, 1992.

Talwani, M., J. L. Worzel, and M. Landisman, Rapid gravity computations for two-dimensional bodies with application to the Mendocino submarine fracture zone, *J. Geophys. Res.*, 64, 49–59, 1959.

Tappert, F. D., and X. Tang, Ray chaos and eigenrays, *J. Acoust. Soc. Am.*, 99, 185–195, 1996.

Tondi, R., R. de Franco, and R. Barzaghi, Sequential integrated inversion of refraction, wide-angle reflection travel times and gravity data for two dimensional velocity structures, *Geophys. J. Int.*, 141, 679–698, 2000.

Virieux, J., et al., Crustal structure underneath Mt. Vesuvius from on land recordings of offshore shots (Mareves '97): Data pre-processing and preliminary interpretation, paper presented at XXII IUGG General Assembly, Birmingham, U.K., 18–30 July, 1999.

Witte, O., M. Roth, and G. Müller, Ray tracing in random media, *Geophys. J. Int.*, 124, 159–169, 1996.

Žáček, K., Smoothing the Marmousi model, *Pure Appl. Geophys.*, 159, 1507–1526, 2002.

Zelt, C. A., and D. A. Forsyth, Modeling wide-angle seismic data for crustal structure: Southeastern Grenville Province, *J. Geophys. Res.*, 99, 11,687–11,704, 1994.

Zelt, C. A., and R. B. Smith, Seismic traveltime inversion for 2-D crustal velocity structure, *Geophys. J. Int.*, 108, 16–34, 1992.

Zollo, A., et al., Seismic evidence for a low-velocity zone in the upper crust beneath Mount Vesuvius, *Science*, 274, 592–594, 1996.

_____

R. de Franco and R. Tondi, Istituto per la Dinamica dei Processi Ambientali (CNR), Via Monte Bianco, 9, I-20131 Milano, Italy. (rosaria.tondi@idpa.cnr.it)